



Title	Development and Exploration of New Materials Related with Carbon and Boron Nitride
Author(s)	田村, 貴大
Citation	北海道大学. 博士(総合化学) 甲第13357号
Issue Date	2018-09-25
DOI	10.14943/doctoral.k13357
Doc URL	<a href="http://hdl.handle.net/2115/71982">http://hdl.handle.net/2115/71982</a>
Type	theses (doctoral)
File Information	Takahiro_TAMURA.pdf



[Instructions for use](#)

# DOCTORAL THESIS

Development and exploration of new materials  
related with carbon and boron nitride

(炭素及び窒化ホウ素系新規材料の開発と物性探索)

Takahiro TAMURA

Materials Chemistry and Engineering Course  
Graduated School of Chemical Sciences and Engineering  
Hokkaido University

( Doctoral Supervisor : Toshihiro SHIMADA, Professor )

( 指導教員 : 島田 敏宏 教授 )

# Contents

Chapter 1 Carbon and Boron Nitride.....	5
1.1 General Introduction.....	5
1.1.1 Characteristics and Differences Between Carbon and Boron Nitride .....	5
1.1.2 Characteristics and Applications of Diamond and cBN.....	7
1.2 Synthesis and Doping Methods .....	12
1.2.1 Diamond .....	12
1.2.2 cBN.....	14
1.3 Problems for Device Applications.....	16
1.4 Objective of This Study .....	17
References .....	19
Chapter 2 Development of New Doping Method for Diamond in Plasma CVD .....	21
2.1 Introduction .....	21
2.2 Experimental Section.....	23
2.2.1 Apparatus and Growth Conditions .....	23
2.2.2 Characterization.....	26
2.3 Results and Discussion .....	26
2.3.1 Surface Morphology and Crystal Structure.....	26
2.3.2 Local Concentration of Boron .....	27

2.3.3 Average Concentration of Boron .....	29
2.3.4 Conductivity at Low Temperature .....	30
2.4 Conclusion .....	31
References .....	32
Chapter 3 Fabrication of Mixed Film of Bismuth and Diamond by Solid Immersion	
Method.....	33
3.1 Introduction .....	33
3.2 Experimental Section.....	34
3.2.1 Apparatus .....	34
3.2.2 Growth Conditions .....	36
3.2.3 Characterization.....	38
3.3 Results and Discussion .....	38
3.3.1 Bismuth Concentration and Crystal Structure .....	38
3.3.2 Surface Morphology .....	41
3.3.3 Effect of Applying Bias .....	41
3.3.4 Microstructure of Films .....	42
3.3.5 Distribution of Bismuth .....	43
3.3.6 Nanostructure of Films .....	44
3.3.7 Structure model .....	46

3.4 Conclusion .....	47
References .....	48
Chapter 4 Surface Scientific Study of cBN .....	50
4.1 Introduction .....	50
4.2 Experimental Section.....	51
4.2.1 Handling of Small cBN Crystals and Their Surface Preparation .....	51
4.2.2 Plasma Processes .....	54
4.2.3 Characterization.....	54
4.3 Results and Discussion .....	55
4.3.1 Plasma Etching of cBN .....	55
4.3.2 Plasma Etching of High-Index Surfaces.....	59
4.3.3 Atomistic Model of the Etching of High-Index Surfaces .....	61
4.3.4 Etching with Solid MgF <sub>2</sub> inserted into Nitrogen Gas Plasma .....	62
4.4 Conclusion .....	67
References .....	68
Chapter 5 Mechanical Properties of Various Index Planes of cBN from Nanoindentation .....	70
5.1 Introduction .....	70
5.1.1 Importance of Elucidating the Mechanical Properties of cBN.....	70

5.1.2 Problems in Nanoindentation of cBN.....	71
5.2 Experimental Section.....	72
5.2.1 Sample Preparation.....	72
5.2.2 Sample Fixing Method .....	73
5.2.3 Indentation Condition .....	76
5.3 Results and Discussions .....	77
5.3.1 Nanoscale Elastic Modulus and Hardness.....	77
5.3.2 Pop-in .....	81
5.3.3 Surface Orientation Dependence of Mechanical Properties.....	82
5.3.4 Mechanical Properties Near Grain Boundary.....	83
5.4 Conclusion.....	86
References .....	88
Chapter 6 General Conclusions .....	89

# Chapter 1 Carbon and Boron Nitride

## 1.1 General Introduction

### 1.1.1 Characteristics and Differences Between Carbon and Boron Nitride

Carbon and boron nitride are materials that have a very similar structure. Various allotropes are known for the both materials which have various properties. Carbon nanotubes, graphene, the diamond and so on are well-known carbon materials. Since the bond of carbon atoms can be changed from one to three dimensional  $sp$ ,  $sp^2$  and  $sp^3$ , it is possible to take a variety of structures. Boron nitride is not as famous as carbon materials, but it has structures similar to carbon materials because it can take a similar bonding network by alternately inserting nitrogen and boron instead of carbon. BN nanotubes corresponding to carbon nanotubes and hexagonal BN (hBN) corresponding to graphene are present. There is also the cBN corresponding to the diamond.

Since the carbon and the boron nitride have similar structures, there are many common points in physical properties such as lightness, high thermal conductivity, hardness, tensile strength and so on. For example, carbon nanotubes have attracted attention as next-generation structural materials due to their lightness and high strength, but BN nanotubes also have comparable strength.

However, not all properties resemble each other. There are also significant differences in electronic properties. Carbon nanotubes and graphene are conductive

materials with very high mobility, but both BN nanotubes and hBN are insulating materials. The conductivity of CNTs and graphene arises due to the freely movable valence electrons not participating in carbon-carbon bonding. On the other hand, in BN nanotubes and hBN, two valence electrons of nitrogen are captured by nitrogen atoms with high electronegativity, and they do not have electrical conductivity [1]. Carbon nanotubes are black because they absorb various wavelength, but BN nanotubes have a large band gap and are white because they transmit light. Compared with carbon, boron nitride are flame retardant materials and have high chemical stability. Figure 1-1 summarizes the features and differences of the general properties of carbon and boron nitride.

It is expected that we can freely change the chemical properties without detracting from excellent structural characteristics by combination between carbon and boron nitride [2], which will lead to a material that can be expected to be useful in various fields of the next generation. At present, methods for mass-producing carbon materials on a commercial scale have been developed [3], but research on mass synthesis of boron nitride material has just begun [4].

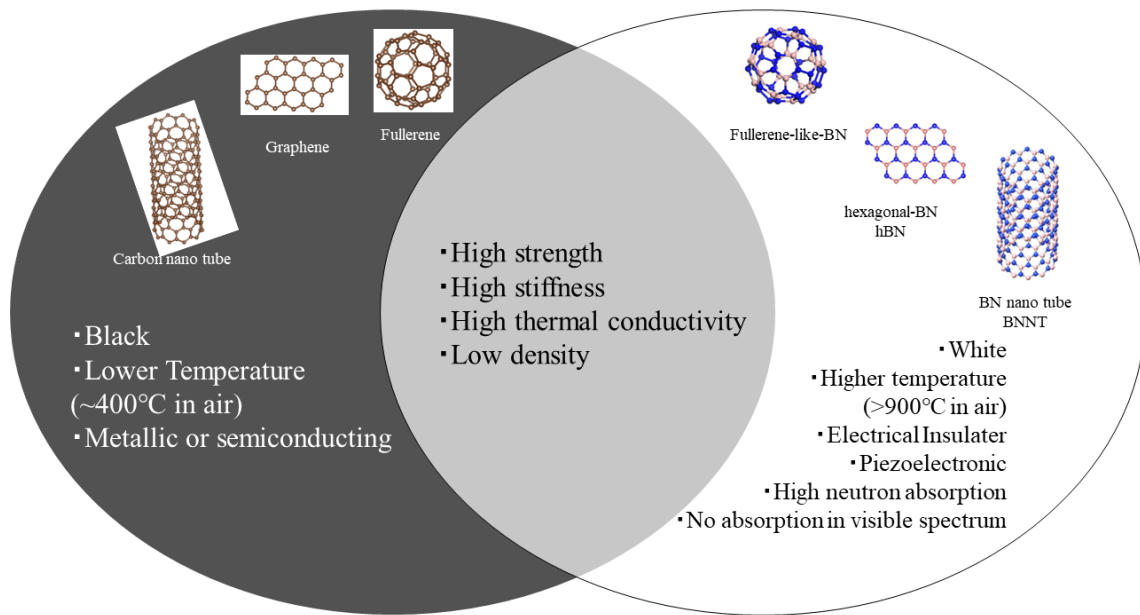


Figure.1-1 Features and differences of the general properties of carbon and boron nitride

### 1.1.2 Characteristics and Applications of Diamond and cBN

The diamond is well known as jewelry or the world's hardest material. The latter is because the network of strong interatomic bonds spread isotopically in three dimensions. Since it has very high thermal conductivity, it has been industrially used as a material that can withstand high stress and heat such as cutting tools and abrasives. The cBN exists as a material having a structure similar to the diamond, and it is a substance having hardness next to the diamond [5]. Unlike carbon and boron nitride allotropes with  $sp^2$  bonding, their electronic properties are very similar. Both are insulators with wide band gap. Table 1-1 shows the properties of the diamond and the cBN.

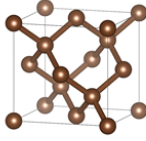
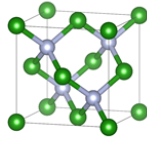
	Diamond	Cubic boron nitride (cBN)
		
Bond length/ Å	1.544	1.565
Density/g cm <sup>-3</sup>	3.515	3.48
Mohs hardness	10	9.5
Thermal conductivity/ W m <sup>-1</sup> K <sup>-1</sup>	2000	1300
Dielectric constant	5.7	7.1
Band gap/ eV	5.47(indirect)	6.2(indirect)
p-,n-type doping	p(easy) n(difficult)	p & n(easy)
Lattice constant / Å	3.566	3.615
Mass-production	○	×

Table 1-1. The properties of the diamond and the cBN.

In recent years, researches have been extensively conducted to add functions to the diamond by doping impurities for the application to various devices. The diamond can be made into a semiconductor from an insulator by doping impurities. It has a wide band gap, high thermal conductivity and carrier mobility. Therefore, it can be applied to low energy consumption, high durability, and small size electronic devices, such as power devices [6], high frequency devices [7], deep ultraviolet LEDs [8], which exceed Si, SiC, GaN and so on. In addition, due to the wide band gap and the low dielectric constant, the free exciton binding energy is large, and free exciton emission can be observed at room temperature. Therefore, it can be used for deep ultraviolet solid state laser source operating at room temperature [9].

It is expected to be applied in various other fields. The nitrogen-vacancy center (NVC) formed by doping the diamond with nitrogen has a function responsive to temperature, magnetic field, electric field, and strain. The NVC can be used as ultra-

sensitive temperature and magnetic field sensor [10]. Because the diamond has good biocompatibility, The NVC can be used as a very small thermometer to sense temperature in living cells and is expected to be useful for establishing new thermal therapy [11]. The diamond is also regarded as an important material in the field of electrochemistry. Boron doped the diamond has conductivity and is used as an electrode for electrochemical reaction. It is characterized by being resistant to decomposition and capable of a very wide electrochemical reaction. Therefore, synthesis of new substances, decomposition / sensing of harmful substances [12] and reduction of CO<sub>2</sub> are actively studied using the diamond electrodes [13]. Many studies have also been reported to explore the special properties of doped the diamond by theoretical calculations. It has been reported that by DFT calculation, transition metal can be doped into the diamond to make it half metal [14] or ferromagnetic [15].

The doping to the diamond may also develop application in quantum information. Because the diamond has a hard lattice and a low dielectric constant, the wave function of the NVC is very insensitive to receive thermal and electrical influences from the outside. Therefore, the doped heterogeneous element behaves as if it were in a vacuum in the diamond. For example, when nitrogen or silicon is doped into the diamond, nitrogen-vacancy defects (NVC) and silicon vacancy defects (SVC) are generated. They can hold spin information for a long time at room temperature and one can read their information by using a laser. Due to this property, the diamond is expected to be applied as a quantum bit used for a quantum computer [16].

However, as will be described later, the diamond has problems before application

in daily life. The diamond is difficult to make n-type conduction, and there is limitation in elements that can be doped into the diamond by gas phase synthesis methods.

On the other hand, it is expected that the cBN is applied in the same way as the diamond by doping. Compared with the diamond, it is easier to make n-type semiconductor by doping, and application as an electronic device is strongly anticipated. Currently, several applied studies using doped cBN have been reported. Fabrication of ultraviolet LEDs of pn junction [17], addition of luminescence by rare earth doping [18], the diamond / cBN heterojunction device fabrication by Si doping [19], and so on. Research on the diamond heterojunction has also been done. A strong stress is applied at the junction interface and a phenomenon unprecedented develops since the diamond and the cBN have lattice constants close to each other and the both have very hard lattices. Recently, the one-dimensional conductivity is developed at the single crystal junction interface between the diamond and the cBN [20]. However, the cBN has a problem with crystal growth technology as described later.

As a summary of the discussion in this section, Table. 1-2 shows the properties and applications of the diamond and the cBN along with other well-known semiconductors.

Table 1-2. Characteristics of semiconductor material

			diamond	cBN	Si	GaAs	3c-SiC	GaN	AlN
Physical property	Lattice constant/Å		3.567	3.615	5.4309	5.653	4.358	a=3.189 c=5.185	a=3.11 c=4.98
	Atomic bond length/Å		1.544	1.565	2.325	2.488	1.888		1.917
	Binding energy /KJ mol <sup>-1</sup>		357		228	163	309		
	Melting point/°C		4000	>3500	1420	1238	2830	2800	2200
	density/g cm <sup>-3</sup>		3.515	3.48	2.328	5.307	3.21	6.1	3.26
	Coefficient of thermal expansion /10 <sup>-6</sup> K <sup>-1</sup>		0.8	3.5	2.4	6	5.12	5.59 3.17	4.3
Mechanical property	Hardness	Mohs	10	9.5	7	4~5	9		9
		Knoop /kgf mm <sup>-2</sup>	7000 ~10000	4500 ~4800			1875 ~3980		1230
	Young's modulus/MPa		7.86	5.2	20		4		3.2
	Sound velocity/m s <sup>-1</sup>		1.8 × 10 <sup>4</sup>		8396	4730	9500	6900	
	Poisson's ratio		0.2	0.2	0.2	0.3	0.2	0.3	0.24
	Thermal property		Specific heat/J g <sup>-1</sup> K <sup>-1</sup>	0.51	0.5	0.75	0.16	0.71	0.49
		Thermal conductivity /W m <sup>-1</sup> K <sup>-1</sup>	2000	1300	163	55	490	1.3 ~2.0	320
Electrical property	Band gap/ eV		5.47	6.2	1.1	1.4	2.3	3.4	6.28
	Mobility (300K) / cm <sup>2</sup> V <sup>-1</sup> s <sup>-1</sup>	Electron	2400		1880	8500	980	900	1100
		Hole	2100		450	420	20	400	
	Saturated electron velocity /10 <sup>7</sup> cm s <sup>-1</sup>		2.7		1.2	2	2	2.7	
	Dielectric constant		5.7	7.1	11.9	13.2	9.7	12	8.7
	Resistivity/ Ωcm		10 <sup>12</sup> -10 <sup>17</sup>	10 <sup>11</sup>	3 × 10 <sup>5</sup>	10 <sup>8</sup>	10 <sup>2</sup> -10 <sup>12</sup>		>10 <sup>14</sup>
	Dielectric breakdown voltage / MV cm <sup>-1</sup>		10-200		3	3.5	10-50	20	11.7
Optical property	Refractive index		2.415 (600nm)	2.117 (589nm)	3.49	3.655	2.65	2.8	2.2

In this research, I have developed new experimental techniques for synthesizing and preparing new materials, surfaces and structures related with the diamond and the cBN and studied their physical and chemical properties.

## **1.2 Synthesis and Doping Methods**

### **1.2.1 Diamond**

As can be seen from the phase diagram (Fig. 1-2), the diamond is a metastable phase in the high pressure phase of carbon. To synthesize this artificially, it is done by applying high temperature and high pressure (HPHT) to the carbon raw material like the environment in which natural the diamond is produced. This method is called HPHT method and has been used for various industrial applications such as synthesis of the diamond fine particles for polishing since the ASEA company in Sweden succeeded in 1955 [21]. In this method, crystals of 10 mm size can be synthesized and used for polishing / cutting tools.

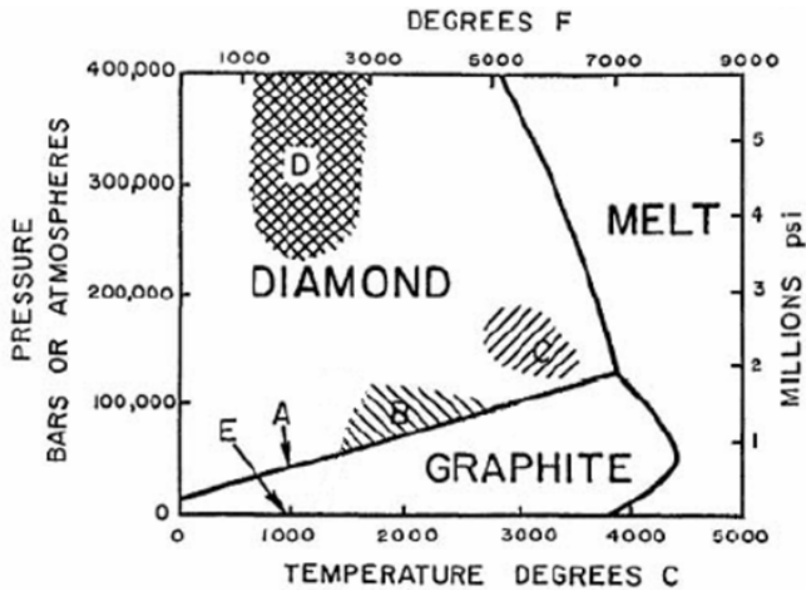


Figure 1-2. The phase diagram of carbon [22].

Low temperature, low pressure gas phase synthesis method of the diamond was developed after HPHT method was developed. Ever since 1960, Mr. W. G. Eversole of Union Carbide of America and Mr. B. V. Derjaguin of the Academy of Sciences of the former Soviet Union succeeded in this method [23] and it has developed since then. Initially, a mixed gas of CO and CO<sub>2</sub> was used, and there was a disadvantage that graphite was generated simultaneously with the diamond. Thereafter, a method using a mixed gas obtained by diluting a carbon gas with a hydrogen gas was developed so as to continuously synthesizing the diamond while etching graphite. Today, methane and hydrogen are used as process gases, and synthesis is carried out by non-equilibrium reaction on the substrate by activating the raw material by heat or microwave (excitation / decomposition of hydrocarbons or formation of atomic hydrogen) has become popular in recent years.

Applied research of the diamond explosively developed after the invention of the gas phase synthesis method. The current mainstream is research on the diamond devices using doped diamonds. There are two methods of the diamond doping, *i.e.*, a gas introduction method and an ion implantation method.

In the gas introduction method, doping is carried out by slightly mixing a gas containing impurities during CVD synthesis. It is carried out by incorporating an impurity element into the diamond lattice at the same time while growing, and it is possible to uniformly doping the entire grown crystal. The disadvantage is that the selectable impurity elements are limited to those that can be gasified, and that they are usually explosive or toxic.

The ion implantation method is a method of doping by implanting impurity element ions into the diamond thin film by accelerating the electric field. Elemental choice is very wide. However, as a few disadvantages, it is inevitable that doping can be performed only on the surface of the diamond and graphite is generated inside the crystal due to high-temperature annealing performed after implantation, resulting in poor crystal quality.

### **1.2.2 cBN**

The phase diagram of boron nitride is shown below (Fig. 1-3). The cBN hardly exists in nature, but it is a high-pressure metastable phase like the diamond, and it can be synthesized by treating nitrogen and boron source under HPHT environment like the diamond.

However, the maximum crystal grain size that can be prepare by this synthesis

method is smaller than that of the diamond, which is about 2 to 3 mm [24]. Precise synthesizing methods of high quality single crystals are studied for the purpose of controlling donors and acceptors of impurity elements for application to electronic devices. At present, there is a report that synthesis of nearly transparent crystals was possible by using Ba solvent [25]. In addition, various element doping by high-temperature high-pressure synthesis method has been attempted, and several synthesis examples of crystals exhibiting p-type and n-type conductivity have been reported [26].

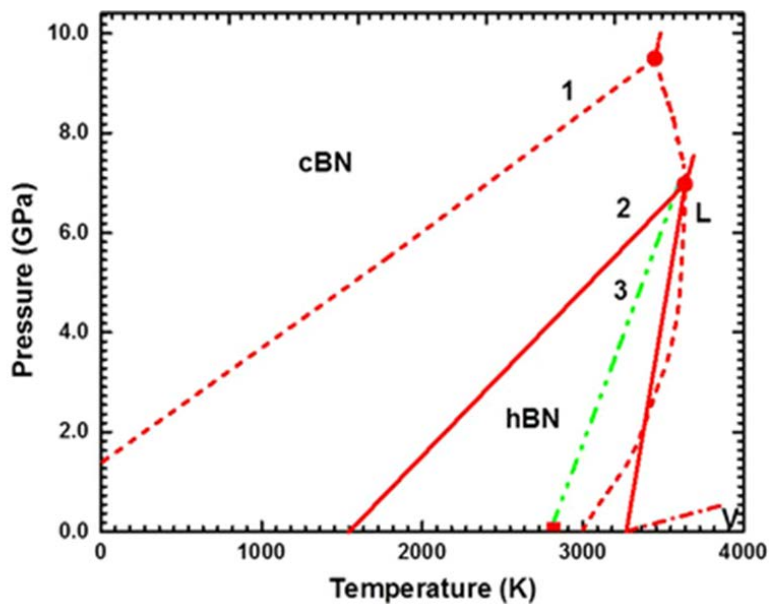


Figure 1-3. The phase diagram of boron nitride [27].

There are many problems to be solved for low pressure gas phase synthesis of the cBN. In the case of CVD using borane, ammonia, nitrogen as the process gas, other BN components (amorphous, turbostratic BN, hexagonal BN, etc.) remain as impurities in the film. Gas containing fluorine, such as  $\text{BF}_3$  [28], has attracted

attention as a gas having an etching effect like hydrogen in the case of the diamond CVD, but the reason why fluorine is effective is unknown. Although it is reported that heteroepitaxial synthesis was successful by the method called IBAD-MBE [29], there is a problem that it is difficult to thicken the film, the apparatus is large scale, and there are few laboratories that can handle it. Although the method called ICP-CVD [30] is also considered to be useful in the study using CVD, the film quality is still polycrystalline, and single crystal growth has not been realized.

Thus, the gas phase synthesis techniques for the cBN is developed only very slowly. One of the reasons is the difficulty of obtaining a single crystal substrate for experiment.

### **1.3 Problems for Device Applications**

Problems in device applications of the diamond and the cBN are summarized below. Regarding the diamond, there are two major problems, one is the problem that n-type the diamond is difficult to synthesize and the other is the problem that there are few methods to make new doped the diamond by gas phase synthesis. Phosphorous is generally used for n-type doping of the diamond. However, controllability of doping using phosphorus is poor. The rate of incorporation of phosphorus into the diamond crystal lattice depends greatly on the plane index. Phosphorus is easily incorporated in the (111) plane direction, but it is difficult to incorporate phosphorus into the (100) plane which is convenient for device fabrication [8]. In addition, since the band gap of the diamond is large and the

dielectric constant is low, the order of the donor is lowered, and the energy necessary for activating the donor is very large as compared with the case of Si. Therefore, a high impurity concentration is necessary for lowering the resistance.

In order to prepare new doped diamonds, it has been experimentally impossible if there is no gas containing the dopant element. Although some new doped diamonds with interesting properties have been discovered by theoretical calculations, it is currently the case that there is no means to synthesize them.

The research on the cBN is hindered by a problem that it is difficult to obtain single crystal substrates for experiments. In fact, compared with the number of academic papers on the diamonds, the number of papers that contain cBN as a concept is less than about 1%. As the research has progressed rapidly since the development of high quality gas phase synthesis of the diamond, the cBN also has the possibility of explosive research as it is discovered.

A method of growing a large area single crystal has not yet been found, and the size of crystals that can be produced by HPHT synthesis method, which is easy to obtain, is as small as about 300  $\mu\text{m}$ . If we can develop a new method to handle these small crystals precisely, it will be a breakthrough in two directions, *i.e.*, homoepitaxy for thin film growth and the indentation for mechanical properties.

## **1.4 Objective of This Study**

As mentioned above, the application of the diamond and the cBN has attracted a lot of attention, but there are many problems concerning the synthesis method and

control of conductivity.

In this thesis, regarding the diamond, I have developed a new doping method usable in the plasma CVD process and verified its effectiveness, and expanded the choice of dopant elements. Based on that method, I also made new the diamond materials using elements that were not combined before.

Subsequently, in order to advance the study of the cBN, I developed a method to easily prepare substrates for experiments. After that, I investigated and clarified the etching reactivity in the plasma of the gas species involved in synthesis, and investigated the mechanical properties important for device application by nanoindentation.

## References

- [1] L. Liu, Y.P. Feng, and Z.X. Shen, *Phys. Rev. B* **68**, 104102 (2003).
- [2] M.B. Jakubinek, B. Ashrafi, J. Guan, K.S. Kim, K.O. Neill, C.T. Kingston, B. Simard, C. Canada, *Nanotech 2015 Conf.* **416** (2015).
- [3] T. Hiraoka, T. Yamada, K. Hata, D.N. Futaba, H. Kurachi, S. Uemura, M. Yumura, and S. Iijima, *J. Am. Chem. Soc.* **128**, 13338 (2006).
- [4] J. Cumings and A. Zettl, *Chem. Phys. Lett.* **316**, 211 (2000).
- [5] C. Stein, M. Keunecke, K. Bewilogua, T. Chudoba, W. Kölker, and H. van den Berg, *Surf. Coatings Technol.* **205**, S103 (2011).
- [6] A. Hiraiwa, H. Kawarada, *J. Appl. Phys.* **114**, 034506 (2013).
- [7] K. Hirama, K. Tsuge, S. Sato, T. Tsuno, Y. Jingu, S. Yamauchi, and H. Kawarada, *Appl. Phys. Express* **3**, 044001 (2010).
- [8] S. Koizumi, K. Watanabe, M. Hasegawa, and H. Kanda, *Science* **292**, 1899 (2001).
- [9] D. Takeuchi, T. Makino, H. Kato, M. Ogura, N. Tokuda, T. Matsumoto, D. Kuwabara, H. Okushi, and S. Yamasaki, *Phys. Status Solidi* **211**, 2251 (2014).
- [10] P. Neumann, I. Jakobi, F. Dolde, C. Burk, R. Reuter, G. Waldherr, J. Honert, T. Wolf, A. Brunner, J.H. Shim, D. Suter, H. Sumiya, J. Isoya, and J. Wrachtrup, *Nano Lett.* **13**, 2738 (2013).
- [11] G. Kucsko, P.C. Maurer, N.Y. Yao, M. Kubo, H.J. Noh, P.K. Lo, H. Park, and M.D. Lukin, *Nature* **500**, 54 (2013).
- [12] K.E. Toghill, G.G. Wildgoose, A. Moshar, C. Mulcahy, and R.G. Compton, *Electroanalysis* **20**, 1731 (2008).
- [13] J.L. DiMeglio and J. Rosenthal, *J. Am. Chem. Soc.* **135**, 8798 (2013).
- [14] E.M. Benecha and E.B. Lombardi, *J. Appl. Phys.* **114**, (2013).
- [15] F. Hussain, M. Ullah, H. Ullah, M. Rashid, M. Imran, and E. Ahmad, *Acta Phys. Pol. A* **127**, 823 (2015).
- [16] F. Jelezko and J. Wrachtrup, *Phys. Status Solidi* **203**, 3207 (2006).
- [17] T. Taniguchi, K. Watanabe, S. Koizumi, I. Sakaguchi, T. Sekiguchi, and S. Yamaoka, *Appl. Phys. Lett.* **81**, 4145 (2002).
- [18] A. Nakayama, T. Taniguchi, Y. Kubota, K. Watanabe, S. Hishita, and H. Kanda, *Appl. Phys. Lett.* **87**, 211913 (2005).
- [19] C.X. Wang, G.W. Yang, T.C. Zhang, H.W. Liu, Y.H. Han, J.F. Luo, C.X. Gao,

- and G.T. Zou, *Diam. Relat. Mater.* **12**, 1422 (2003).
- [20] C. Chen, Z. Wang, T. Kato, N. Shibata, T. Taniguchi, and Y. Ikuhara, *Nat. Commun.* **6**, 6327 (2015).
- [21] H. Liander and E. Lundblad, *ASEA Journal* **28**, 97 (1955).
- [22] F.P. Bundy, *Science* **137**, 1057 (1962).
- [23] J.C. Angus and C.C. Hayman, *Science* **241**, 913 (1988).
- [24] H. Saito and Y. Yukio, *J. Chem. Inf. Model.* **53**, 1689 (2013).
- [25] T. Taniguchi and K. Watanabe, *J. Cryst. Growth* **303**, 525 (2007).
- [26] W.J. Zhang, Y.M. Chong, I. Bello, and S.T. Lee, *J. Phys. D. Appl. Phys.* **40**, 6159 (2007).
- [27] J. Narayan and A. Bhaumik, *Metall. Mater. Trans. A*, **47**, 1481 (2016).
- [28] W.J. Zhang, C.Y. Chan, K.M. Chan, I. Bello, Y. Lifshitz, and S.T. Lee, *Appl. Phys. A Mater. Sci. Process.* **76**, 953 (2003).
- [29] K. Hirama, Y. Taniyasu, S.I. Karimoto, H. Yamamoto, and K. Kumakura, *Appl. Phys. Express* **10**, 3 (2017).
- [30] K. Teii, *IEEE Trans. Plasma Sci.* **42**, 1 (2014).

# **Chapter 2 Development of New Doping Method for Diamond in Plasma CVD**

## **2.1 Introduction**

The variety of thin film materials and devices is continuously increasing because of the incessant development of their deposition techniques [1]. It has become possible to control the nanoscale integration of various materials including semiconductors, metals, oxides, organic molecular materials, and polymers [2-6], which has enabled high-performance and lightweight devices with new functions, yet allowing resource savings. Various novel thin film devices using doped the diamonds have emerged recently, which include highly B-doped the diamonds showing superconductivity [7,8], deep-UV LEDs fabricated from the diamond p-n junctions[9], single photon sources realized by isolated NV centers in the diamonds[10]. These unique functions of the devices originate mainly from the wide band gap and the ultra-hard lattice of the diamonds, which create distinctive dopant states. Theoretical investigations predict that there are plenty of novel doped the diamonds that have never been synthesized, such as n-type the diamonds by co-doping of multiple elements [11, 12]. Despite the long history of the doped the diamonds [13], the synthesis of novel doped the diamonds is worth pursuing. Three methods are commonly used to fabricate doped the diamonds: chemical vapor deposition (CVD) growth with gas-phase dopants, dopant ion implantation to a diamond crystal, and a spray mist supply of dopant solution. It is difficult to explore

the full possibility of doped the diamonds by these methods because of their many limitations. Although the doping of light elements such as B, N, and P is possible by introducing gas-phase dopants ( $(\text{CH}_3)_3\text{B}$ ,  $\text{NH}_3$ , and  $\text{PH}_3$ , respectively) during plasma CVD, the handling of these dopant gases is difficult and costly owing to their very toxic and flammable nature. Many elements do not have volatile compounds from the beginning. The ion implantation is a more versatile technique, but it requires annealing to settle the interstitial dopant atoms in the crystal lattice. The material approaches thermal equilibrium by annealing, which expels the dopants above a certain concentration. This diminishes the flexibility of the dopant choice and the maximum concentration. The ion implantation also has a drawback of inhomogeneous doping in the depth direction. The spray mist supply of dopants has been used only for boron doping in the literature [14]. It is very convenient but may have problems of impurity or aggregation of the dopants. To eliminate these limitations, I attempted doping of the diamond using solid sources, *i.e.*, by immersing a polycrystalline boron rod into the  $\text{H}_2\text{-CH}_4$  plasma during the microwave plasma-assisted CVD (MPCVD) of the diamonds. This method is free from the limitations of the currently used techniques because it does not use gaseous dopants nor requires annealing. The grown films were characterized by X-ray diffraction (XRD), Raman spectroscopy, glow discharge optical emission spectroscopy (GDOES), and electrical conductivity measurements.

## 2.2 Experimental Section

### 2.2.1 Apparatus and Growth Conditions

A center-antenna-type MPCVD equipment (Arios Inc., DCVD-51A) was used for the growth of thin the diamond films. Microwave energy (2.45 GHz) from a solid-state power supply was emitted from the antenna rod sticking out at the center of a spherical chamber. The microwave energy is reflected by the inner wall of the spherical chamber made of stainless steel and resonates. The sample holder ( $\phi$  10 mm molybdenum) was placed on the antenna rod. The microwave power was concentrated at the sample holder, and plasma was ignited in the H<sub>2</sub>-CH<sub>4</sub> atmosphere. The intense plasma was limited within a spherical area of 15-mm diameter, which enables the diamond synthesis at low power (ca. 200 W). This equipment also has the merit of low contamination because the plasma does not touch the chamber wall. I modified the equipment by attaching a linear motion to insert a boron rod ( $\phi$  6 mm  $\times$  L 30 mm) along the vertical direction from the sample normal (Fig. 2-1). The electrostatic potential of the boron rod and the sample holder can be modified separately up to  $\pm$  500 V from the chamber wall. The temperature was monitored by a radiation thermometer (Minolta TR-630A, using the emissivity 0.75 for Si and 0.95 for the diamond).

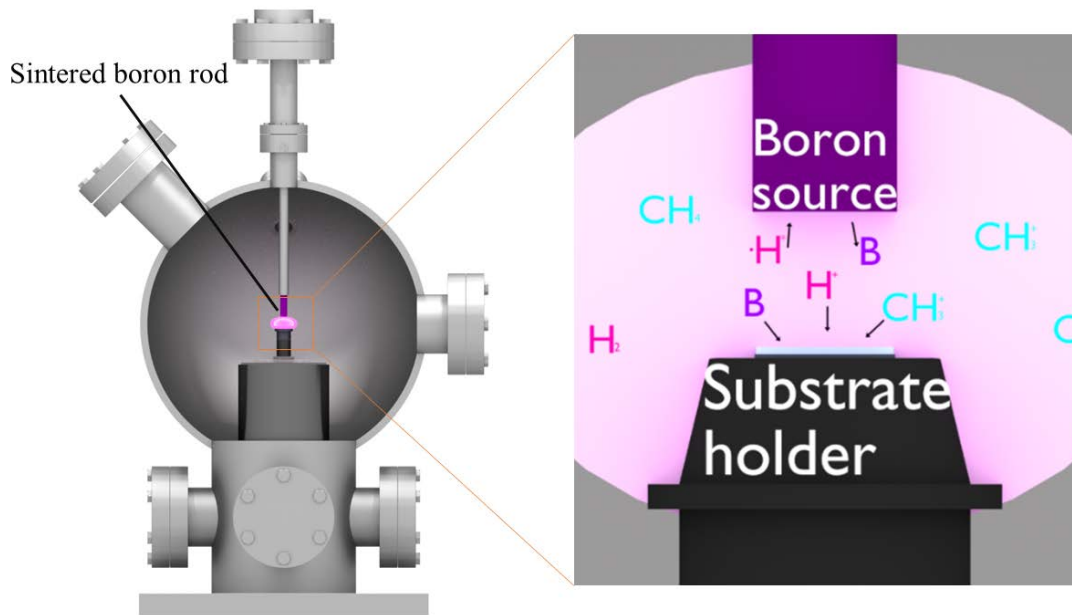


Figure 2-1. Cross-sectional drawing of MPCVD chamber with solid-state dopant and schematics of solid immersion doping.

In the diamond growth experiment, I used substrates of a high resistivity Si (100) wafer (cut into 5-10 mm square) and the diamond (100) single crystals ( $2.5 \times 2.5 \times 0.2 \text{ mm}^3$ ). The Si wafers were cleaned by the RCA method to remove contamination. The diamond (100) crystals were cleaned by  $\text{H}_2$  gas plasma at  $1000 \text{ }^\circ\text{C}$  with 6 kPa  $\text{H}_2$  discharged by 200 W microwave energy for 6 h to remove  $\text{sp}^2$  components. To grow thin the diamond films on Si, the nucleation was enhanced by applying a static bias (-300 V) [15] to the sample for the initial 30 min of MPCVD in  $\text{CH}_4 : \text{H}_2 = 6 \% : 94 \%$  and a total pressure of 3 kPa. This procedure was omitted for the growth on the diamond (001) surfaces.

The growth condition of the B-doped the diamond was optimized to obtain the largest crystalline grains as follows:  $\text{CH}_4 : \text{H}_2 = 1.2 \% : 98.8 \%$ , total pressure was 6

kPa, the surface temperature was 1000 °C, and the surface cleaning and the nucleation procedure were as stated above. The boron rod, penetrating into the plasma along the vertical direction from the sample normal, was placed at 15 mm from the sample surface. This distance is the optimized one for the uniformity of the plasma and the maximum doping concentration. Figure 2-2 shows the optical image of the sample and the boron rod during the MPCVD growth. The growth was continued for 24 h. I applied +450 V against the chamber wall to both the sample holder and the boron rod in order to avoid carbon contamination of the boron surface and enhance the growth of the diamond. If the positive bias is not applied to the boron rod, the surface of the rod becomes dusty owing to the growth of carbon species.

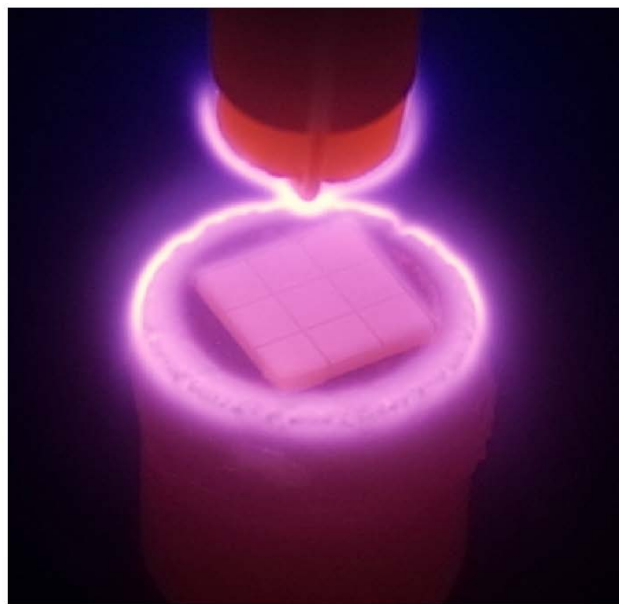


Figure 2-2. Optical image of the sample and the boron rod.

### **2.2.2 Characterization**

The surface morphology was studied by the laser optical microscope images (Keyence VK-8710).

The crystal structure was characterized by XRD (Rigaku RINT-2000).

The concentration of boron in the samples was studied by analysed by Raman microscopy (Renishaw inVia Raman microscope, 5  $\mu$  m spot size, 532 nm excitation).

The average concentration of boron in the diamond film was studied by Glow Discharge Optical Emission Spectrometry (GDOES). The reference sample which determine concentration of B / C was sintered B<sub>4</sub>C pellet (6  $\phi$   $\times$  3mm).

The conductive properties of low temperature were measured by PPMS (Quantum Design).

## **2.3 Results and Discussion**

### **2.3.1 Surface Morphology and Crystal Structure**

Figure 2-3 shows the laser optical microscope images (Keyence VK-8710) of the boron-doped the diamond on Si (001) and the diamond (001). Microcrystalline films with 10- to 50- $\mu$ m crystal grains were obtained on both substrates. XRD was obtained from the sample grown on Si (001) to examine the crystallinity of the film (Fig. 2-4). It was confirmed that the diamond crystals were grown without graphite or other carbon allotropes.

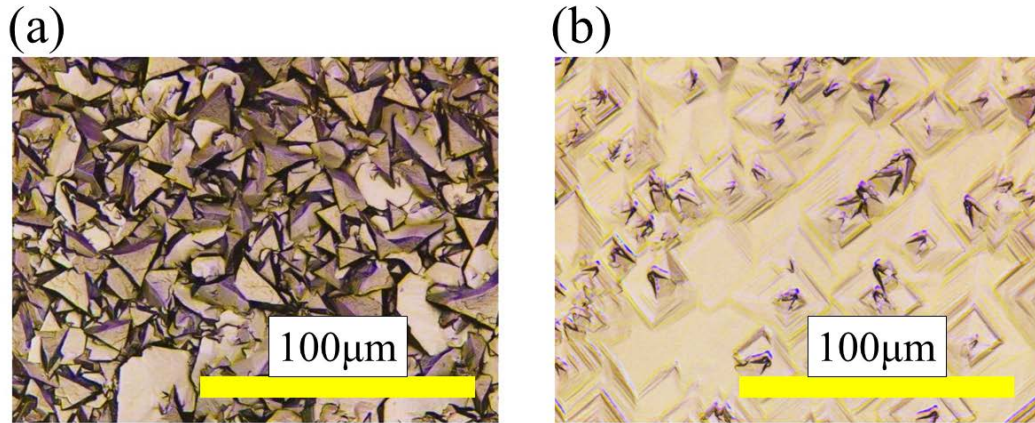


Figure 2-3. Laser microscope images of the diamond film grown on (a) Si(001) and (b) the diamond (001).

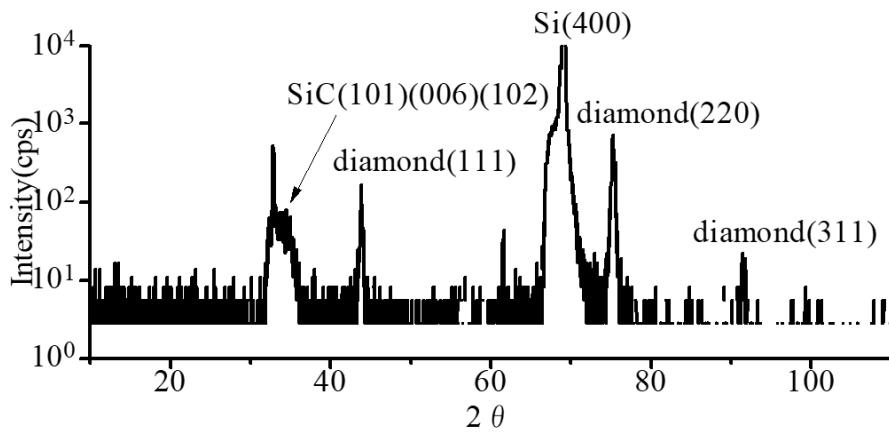


Figure 2-4. X-ray diffraction of boron-doped the diamond grown on Si(001).

### 2.3.2 Local Concentration of Boron

I next characterized the sample grown on Si(100) by Raman microscopy

(Renishaw InVia with 532 nm excitation). It is reported that Raman peak shapes are strongly dependent on boron concentration and that they can be used to estimate boron concentration [16, 17]. The Raman spectra differed considerably from position to position on the  $6 \times 6 \text{ mm}^2$  sample. The measured areas were 2- $\mu\text{m}$  spots in 5-30  $\mu\text{m}$  crystalline grains. The center position exhibited two peaks at 480 and 1250  $\text{cm}^{-1}$  (Fig. 2-5(a)) that are characteristic of boron-doped the diamond (111). By comparing the spectrum shapes with those in the literature [16, 17], the boron concentration at this position was estimated to be 1%. Figure 2-6 is an optical microscope image at a position measured by a Raman microscope. As can be seen from Fig. 2-6, the diameters of the diamond grains are small at the center and large at the outer edge.

The boron concentrations at the sample edge (Fig. 2-5(b)) and the sample corner (Fig. 2-5(c)) were estimated to be 0.5 % and 0.02 %, respectively. The distribution of the boron concentration was almost concentric, although the boron rod was immersed unsymmetrically relative to the sample normal. This is because the distance between the boron rod and the sample surface was regulated so as not to disturb the spherical symmetry of the plasma. Therefore, the reason for this inhomogeneity of the boron concentration is related to the fact that the growth speed is faster near the periphery of the samples.

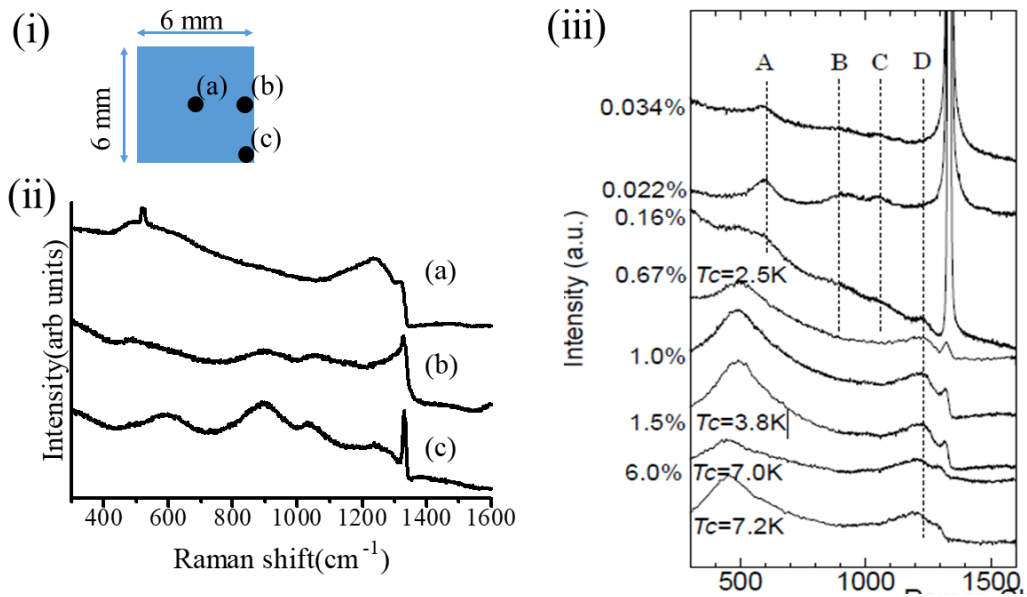


Figure 2-5. (i) Measurement point on the substrate. (ii) Raman spectra of a boron-doped diamond at different positions. (a) center, (b) edge, (c) corner. (iii) Relationship between boron concentration and Raman spectrum [16, 17].

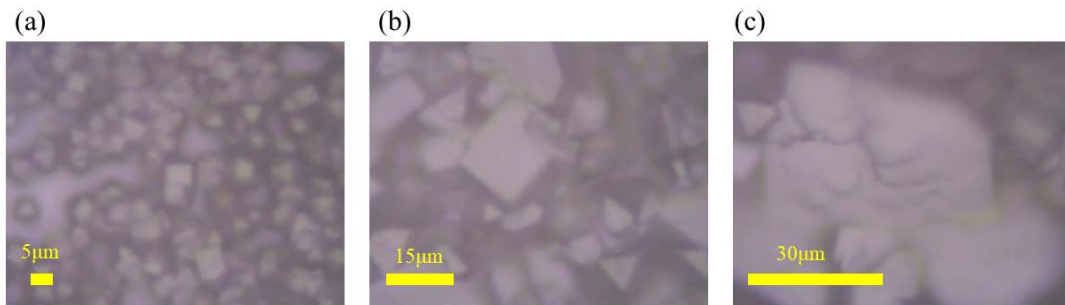


Figure 2-6. An optical microscope image at the position measured by a Raman microscope.

### 2.3.3 Average Concentration of Boron

I measured the boron concentration in the diamond by GDOES (Horiba Jobin Yvon GD-Profilier). This method quantifies the intensity of element-specific optical

emission of sputtered atoms by Ar glow discharge. I used a sintered polycrystalline B<sub>4</sub>C disc as the standard material to derive the B / C ratio in the diamond; B : C = 0.5 % : 99.5 %. Because the GDOES measures the whole sample (4 mm  $\phi$ ) as average, this result agrees well with the Raman results.

### **2.3.4 Conductivity at Low Temperature**

To study the electronic properties of the boron-doped the diamond films, I measured electrical conductivity at low temperature. I attached four electrodes on a 6-mm square sample grown on highly resistive Si(001) and measured the conductivity down to 1.8K (Quantum Design PPMS). The thickness of the B-doped the diamond film was 10  $\mu\text{m}$  with a 20  $\mu\text{m}$  buffer (and insulation) layer of undoped the diamond. Note that the sample contained regions of various B concentrations as shown in Fig. 2-5. I measured many samples and the result showing the lowest resistivity at low temperature is shown in Fig. 2-6. It shows relatively low resistivity of approximately  $1.5 \times 10^{-2} \Omega\text{cm}$ . This value is low enough for electrochemical applications [18, 19]. The resistivity increased when the temperature decreased from 300 to 60 K but decreased when the temperature decreased below 60 K. This strange behavior, including a steep decrease below 2.5 K, seems to arise from the inhomogeneity of the boron concentration in the film. Attempt to prepare smaller samples for better uniformity to observe the superconductive zero-resistivity was not successful.

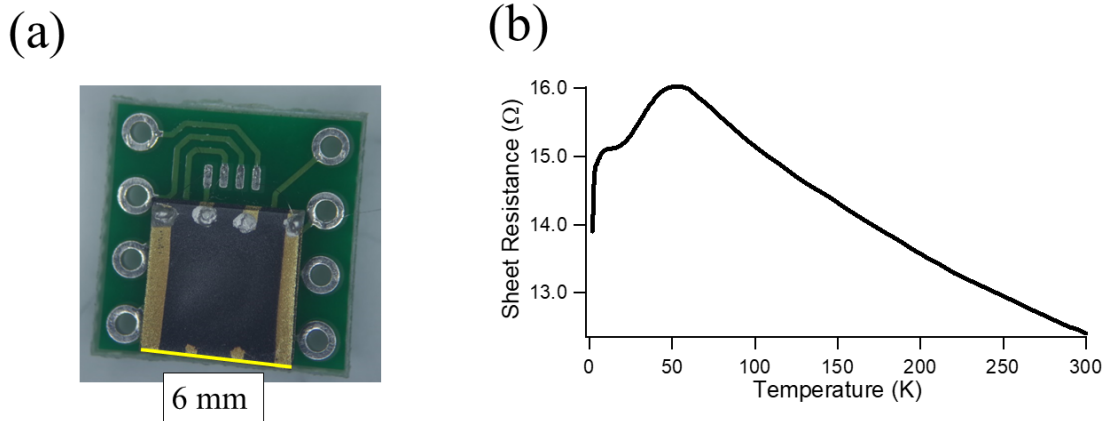


Figure 2-6. (a) Device configuration. (b) Sheet resistance of a boron-doped the diamond film (thickness 10  $\mu\text{m}$ ) grown on an undoped the diamond buffer layer (thickness 20  $\mu\text{m}$ ) on Si(001).

## 2.4 Conclusion

In summary, I developed a new technique to grow doped thin the diamond films. The method involves simply immersing the solid dopant source into the plasma during MPCVD to sputter and atomize the dopant elements. I demonstrated the doping of boron from a sintered boron rod and characterized the sample by XRD, Raman microscopy, and GDOES. I found that 1% B-doping was possible, but the concentration of boron was rather inhomogeneous, with a distribution ranging from 1% to 0.02% within a 10-mm sample. This technique is suitable for examining the possibility of doping of various elements including multiple dopants.

## References

- [1] K. Ariga, Y. Yamauchi, G. Rydzek, Q. Ji, Y. Yonamine, K. C. W. Wu, J. P. Hill, *Chem. Lett.* **43**, 36 (2014).
- [2] K. Togashi, Y. Sagara, T. Yasuda, C. Adachi, *Chem. Lett.* **42**, 651 (2013).
- [3] Y. Muronoi, J. Zhang, M. Higuchi, H. Maki, *Chem. Lett.* **42**, 761 (2013).
- [4] M. Kawasaki, *Bull. Chem. Soc. Jpn.* **86**, 1341 (2013).
- [5] Y. Shimakawa, *Bull. Chem. Soc. Jpn.* **86**, 299 (2013).
- [6] Y. Matsuo, *Chem. Lett.* **41**, 754 (2012).
- [7] Y. Takano, M. Nagao, I. Sakaguchi, M. Tachiki, T. Hatano, K. Kobayashi, H. Umezawa, H. Kawarada, *Appl. Phys. Lett.* **85**, 2851 (2004).
- [8] T. Muranaka, K. Kobashi, H. Okabe, T. Tachibana, Y. Yokota, K. Hayashi, N. Kawakami, J. Akimitsu, *Diam. Relat. Mater.* **20**, 1273 (2011).
- [9] S. Koizumi, K. Watanabe, M. Hasegawa, H. Kanda, *Science* **292**, 1899 (2001).
- [10] N. Mizuochi, T. Makino, H. Kato, D. Takeuchi, M. Ogura, H. Okushi, M. Nothaft, P. Neumann, A. Gali, F. Jelezko, J. Wrachtrup, S. Yamasaki, *Nat. Photonics* **6**, 299 (2012).
- [11] U. Schwingenschlögl, A. Chroneos, C. Schuster, R. W. Grimes, *J. Appl. Phys.* **110**, 056107 (2011).
- [12] R. J. Eyre, J. P. Goss, P. R. Briddon, M. G. Wardle, *Phys. Status. Solidi. A* **204**, 2971 (2007).
- [13] R. Kalish, *Carbon* **37**, 781 (1999).
- [14] T. Yano, D. A. Tryk, K. Hashimoto, A. Fujishima, *J. Electrochem. Soc.* **145**, 1870 (1998).
- [15] S. Yugo, T. Kanai, T. Kimura, T. Muto, *Appl. Phys. Lett.* **58**, 1036 (1991).
- [16] R. J. Zhang, S. T. Lee, Y. W. Lam, *Diam. Relat. Mater.* **5**, 1288 (1996).
- [17] T. Watanabe, T. K. Shimizu, Y. Tateyama, Y. Kim, M. Kawai, Y. Einaga, *Diam. Relat. Mater.* **19**, 772 (2010).
- [18] A. Suzuki, T. A. Ivandini, K. Yoshimi, A. Fujishima, G. Oyama, T. Nakazato, N. Hattori, S. Kitazawa, Y. Einaga, *Anal. Chem.* **79**, 8608 (2007).
- [19] K. Nakata, T. Ozaki, C. Terashima, A. Fujishima, Y. Einaga, *Angew. Chem. Int. Ed.* **53**, 871 (2014).

# **Chapter 3 Fabrication of Mixed Film of Bismuth and Diamond by Solid Immersion Method**

## **3.1 Introduction**

There are various carbon materials; *i.e.*, graphene, carbon nanotube, fullerene, and the diamond. The variation is still increasing with the addition of less-common allotropes including chaoite [1, 2], carbyne [3], compressed super hard graphite [4], m-carbon [5], bct-C<sub>4</sub> [6], and z-carbon [7], which are experimentally identified or theoretically predicted. The condition of their formation and physical and chemical properties of them are not fully understood. This chapter reports the formation of unusual carbon-containing solid during attempts to synthesize bismuth-doped the diamond by plasma CVD. Doped the diamonds are attractive for various exceptional applications [8–11], but it is extremely difficult except for a very few number of elements, such as B, N and P. Since the efficient dopants and their combinations are still being developed for various applications, a simple and versatile technique for the doping of the diamond is needed. I here present an attempt to dope bismuth in the diamond. If the bismuth doping becomes possible, a good n-type the diamond semiconductor might be obtained because the binding energy of the outmost electron decreases as the element size increases. However, this relation does not hold true for P and As in the diamond [12]. Clarifying this issue is important for the semiconductor application of the diamond. Even if the doping of bismuth to the diamond lattice is impossible, the composite material between bismuth and the

diamond may be useful because of the catalytic function of CO<sub>2</sub> reduction and electrochemical metal sensing ability of bismuth [13,14] combined with electrochemical functions of boron-doped the diamond [15]. Popular methods for the doping of the diamond are as follows: (1) using gaseous compounds of dopants [16], or (2) ion implantation followed by annealing [17]. Method (1) has a problem of using toxic gases, whereas method (2) has the problem of a low throughput. I developed a simple and versatile method to supply foreign elements during the plasma CVD, *i.e.*, the solid source immersion in the plasma for the diamond CVD [18], which is similar to the method developed by Kohn et al. for delta-doping [19]. This method has an advantage of supplying various elements with a high concentration without the problems stated above. I examined the films by XRD, XRF, Raman spectroscopy, isotope microscopy and TEM.

## **3.2 Experimental Section**

### **3.2.1 Apparatus**

I used compact microwave plasma CVD equipment which uses a microwave antenna as the sample holder (ARIOS DCVD-51A-SSP). A movable rod was vertically attached to this equipment to immerse the solid source (Fig. 3-1(a)).

The materials I used as substrates were Si substrates ((100) orientation, 5 × 5 mm), single crystal the diamond substrates ((100) oriented, 2.5 × 2.5 mm) and Mo grids for the TEM analysis. The Si substrates were cleaned by the RCA method and scratched by nano-diamond powder in ethanol in an ultrasonic bath for nucleation. The single crystal the diamond substrate was cleaned by an H<sub>2</sub> plasma. The Mo grids

were pretreated by the bias enhanced nucleation (BEN) method [20]. The MW power, total pressure, gas ratio and bias voltage were maintained at 200 W, 3000 Pa, CH<sub>4</sub>/H<sub>2</sub> = 10 % and -200 V, respectively. The BEN treatment time was 30 min. The substrate holder was made of graphite, because there is a report on abnormal the diamond grain growth using a Mo substrate holder [21], and the graphite is easily machined to the designed shape. A specially designed apparatus for immersing the bismuth was attached to the end of the movable rod. Figure 3-1(b) shows the cross section of this apparatus. The bismuth container was a cylinder made of stainless steel ( $\phi$  4 mm  $\times$  25 mm). The open end of this cylinder is covered by a lid made of carbon and W wire. By using this apparatus, I can supply bismuth to the plasma in a stable manner for a long time (~24 h) without dropping as a liquid. Bismuth is an element of a low-melting point (271.4 °C) and it melts by the plasma heat and is released from the opening between the reservoir and the lid like ink from a fountain pen. The distance between the bismuth source and the plasma ball is variable, and I have established a calibration procedure to obtain stable results about the bismuth concentration. Figure 3-1(c) shows the optical image of the sample and inserted rod in plasma. The blue light emission corresponding to Bi ( $472.25 \text{ nm} \cdot {}^2D_{3/2} \rightarrow {}^3P_{1/2}$ ) indicates evaporation of the bismuth [22]. It shows that I can constantly supply Bi at a high concentration. The flow rates of the source gases (H<sub>2</sub> and CH<sub>4</sub>) were electronically regulated by mass flow controllers. The substrate was heated by microwaves and its temperature was measured by a radiation thermometer. The typical temperature was 1050 °C

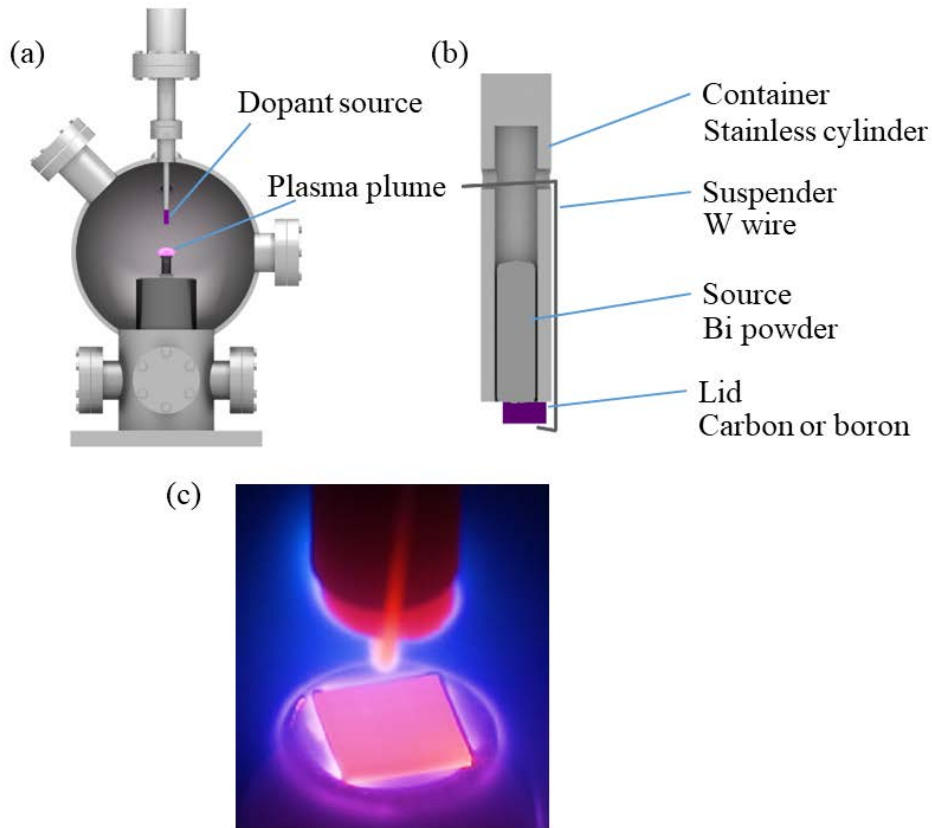


Figure 3-1. (a) Cross sectional drawing of MPCVD chamber with solid state dopant immersion. (b) Cross sectional drawing of the bismuth container attached to the end of a movable rod. (c) Optical image of the sample and rod during the CVD growth.

### 3.2.2 Growth Conditions

I initially grew intrinsic poly-crystalline the diamond films on the Si substrate to prevent a possible reaction of Bi with Si (~15  $\mu\text{m}$  thick). I then inserted the bismuth source into the plasma and applied several bias voltage patterns to the substrate. The growth conditions of the intrinsic the diamond CVD were optimized to quickly growth the diamond with a good crystallinity. The growth rate was 0.8  $\mu\text{m}/\text{h}$ . The detailed growth conditions and sample descriptions are summarized in Tab. 3-1 and

3-2, respectively. The applied bias voltage was changed to determine how the bismuth was included in the films. No bias was applied in condition (a). Positive bias was constantly applied in condition (b). A negative bias was constantly applied in condition (c). An alternating bias was used in condition (d). I prepared three types of samples with different growth conditions for the TEM analysis. The sample (d-i) was pre-treated for nucleation by the BEN method and grown in the mixture gas containing CH<sub>4</sub>, H<sub>2</sub>, Ar, just as for the Si and the diamond substrates. The sample (d-ii) was not treated for nucleation and grown in the mixture gas containing CH<sub>4</sub>, H<sub>2</sub> and Ar. The sample (d-iii) was not treated for nucleation and grown in the mixture gas only containing H<sub>2</sub> and Ar.

Table 3-1. The CVD growth conditions.

	Normal CVD	Bismuth immersed CVD
Gas flow rate (sccm)		
H <sub>2</sub>	80	80
CH <sub>4</sub>	1	1
Ar	80	80
substrate temperature (°C)	1000	900~1000
Pressure (Pa)	$6.5 \times 10^3$	$6.5 \times 10^3$
Bias voltage (V)	-	*
Distance between the substrate and the tip of rod (mm)	-	4~7
Duration (hour)	24	24

Table 3-2. the samples

sample	Bias voltage(V)	Substrate	Source gasses	nucleation
(a)	0	Si	CH <sub>4</sub> , H <sub>2</sub> , Ar	Powder treatment
(b)	+200	Si	CH <sub>4</sub> , H <sub>2</sub> , Ar	Powder treatment
(c)	-200	Si	CH <sub>4</sub> , H <sub>2</sub> , Ar	Powder treatment
(d)	-200±+200	Si	CH <sub>4</sub> , H <sub>2</sub> , Ar	Powder treatment
(d')	-200±+200	Single crystal diamond	CH <sub>4</sub> , H <sub>2</sub> , Ar	-(H <sub>2</sub> plasma cleaning)
(d'')	-200±+200	Single crystal diamond	CH <sub>4</sub> , H <sub>2</sub> , Ar	-(H <sub>2</sub> plasma cleaning)
(d-i)	-200±+200	Mo mesh	CH <sub>4</sub> , H <sub>2</sub> , Ar	BEN
(d-ii)	-200±+200	Mo mesh	CH <sub>4</sub> , H <sub>2</sub> , Ar	-
(d-iii)	-200±+200	Mo mesh	H <sub>2</sub> , Ar	-

### 3.2.3 Characterization

The concentration of bismuth in the samples was analyzed by X-ray fluorescence (JEOL JSX-3100R II, 50 kV). The surface morphology was studied by laser microscopy (KEYENCE VK-8710). The crystal structure was characterized by XRD (Rigaku RINT-2000). The local structure was analysed by Raman microscopy (Renishaw inVia Raman microscope, 5 µm spot size, 785 nm excitation). This 785 nm excitation is appropriate to observe graphite species including the diamond and impurities [23]. The nanoscale structure and composition were examined by TEM with EDS (JEOL JEM-2010). The in-plane distribution and depth profile of Bi was analysed using an isotope microscope, *i.e.*, microprobe SIMS with imaging functions [24].

## 3.3 Results and Discussion

### 3.3.1 Bismuth Concentration and Crystal Structure

Figure 3-2(a)–(c) shows the result of XRF data results for the growth conditions

(a)–(c) in Tab. 3-2. Bismuth was detected only from sample (c). It is thus considered that the negative bias voltage promotes the inclusion of the bismuth into the diamond films. Figure 3-3(a)–(c) shows the corresponding XRD data. Sample (a) contained graphite, SiC and the diamond. Sample (b) contained the diamond and SiC only. Generally, SiC was observed as a by-product from the CVD the diamond films on Si [25]. However, sample (c) was composed of the diamond with a graphitic impurity. Therefore, I attempted a new sequence of applying bias to the substrate. For the new condition (d), the polarity of the bias was alternately switched every 30 s. As a result, bismuth was also detected in sample (d) (Fig. 3-2(d)). As for the graphitic impurity detected by XRD, the ratio of graphitic / the diamond species in sample (d) was about 1/5 of sample (c). The depth profile of bismuth in sample (d), possibly caused by alternating the bias voltage, will be discussed later.

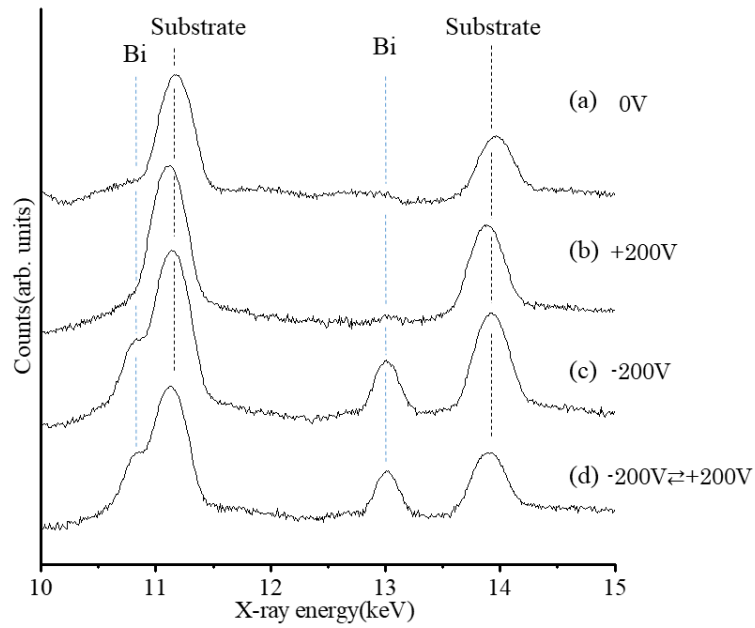


Figure 3-2. Results of XRF. (a)–(d) correspond to the growth conditions in Tab. 3-2

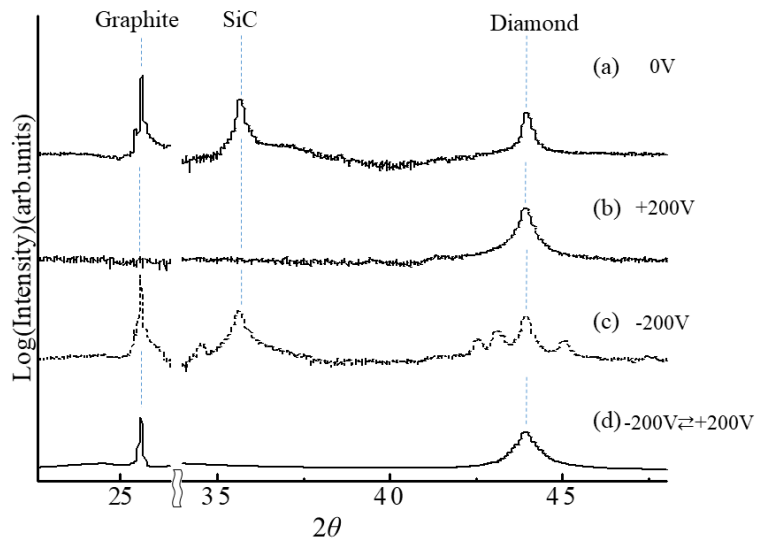


Figure 3-3. Results of XRD. (a)–(d) correspond to the growth conditions in Tab. 3-2. Strong signals from the substrates are observed in the region between  $2\theta = 27\text{--}34^\circ$ .

### 3.3.2 Surface Morphology

The laser microscopy data of Fig. 3-4(a) shows the surface morphology of the bismuth-immersed sample grown on the single-crystal the diamond substrate by an alternating bias (sample (d') in Tab. 3-2). The surface of the sample was rough with non-epitaxial grains. In contrast, epitaxial grains were observed in Fig. 3-4(b) that shows the sample growth without immersing bismuth in the plasma (sample (d'') in Tab. 3-2). It indicated that immersing bismuth enhances the abnormal grain growth.

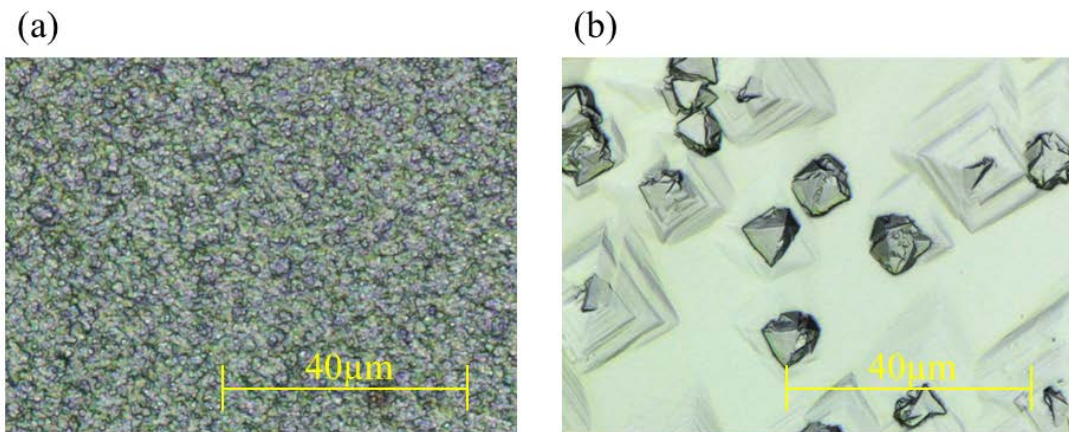


Figure 3-4. Surface morphology of the sample grown on the single crystal the diamond substrate with alternating bias. (a)With bismuth immersion. (b)Without bismuth immersion.

### 3.3.3 Effect of Applying Bias

Generally, applying a positive bias to the substrate is used for enhancing the growth of the diamond, because the positive bias enhances the reactivity of the hydrogen radical on the surface of the substrate and increases the etching rate of the graphitic species [26]. On the other hand, applying a negative bias to the substrate

increases the frequency of the ion bombardment. The ion bombardment causes etching of the diamond and accelerates the synthesis of  $sp^2$  carbon species (*i.e.*, graphite). It results in graphitic impurities in the sample remaining without being etched. However, the result of samples (d) and (d') (the sample using the diamond substrate) indicated that applying an alternating bias is effective to decrease the amount of graphitic impurities and incorporating bismuth into the film.

### 3.3.4 Microstructure of Films

Figure 3-5 shows the results of the Raman microscopy. Spectra taken from the sample grown with bismuth showed several different shapes depending on the position of the sample. The spectrum taken from the area of the flat crystal surface (Fig. 3-5(a)) had a smooth shape with the diamond peak ( $1332\text{ cm}^{-1}$ ). The poor crystallinity of the diamond seen from the broad background is probably due to the supply of Ar gas in the plasma, which will be discussed later. On the other hand, the spectrum taken from the area containing grain boundaries shows many peaks (Fig. 3-5(b)). It indicates the existence of a molecule-like carbon species or bismuth-carbon compounds at the grain boundaries. An example of a molecule-like carbon species is a diamondoid, *i.e.*, a molecule composed of carbon with the  $sp^3$  structure ( $C_{4n+6}H_{4n+12}$ ,  $n = 1-5$ ), which shows Raman spectra with many peaks [27-29]. Another possibility is Bi and C cluster molecules. Although there are no reports on the crystalline compounds of Bi and C to the author's knowledge, there are some reports on cluster molecules made of bismuth and carbon [30-32]. Raman measurements of them have not been made.

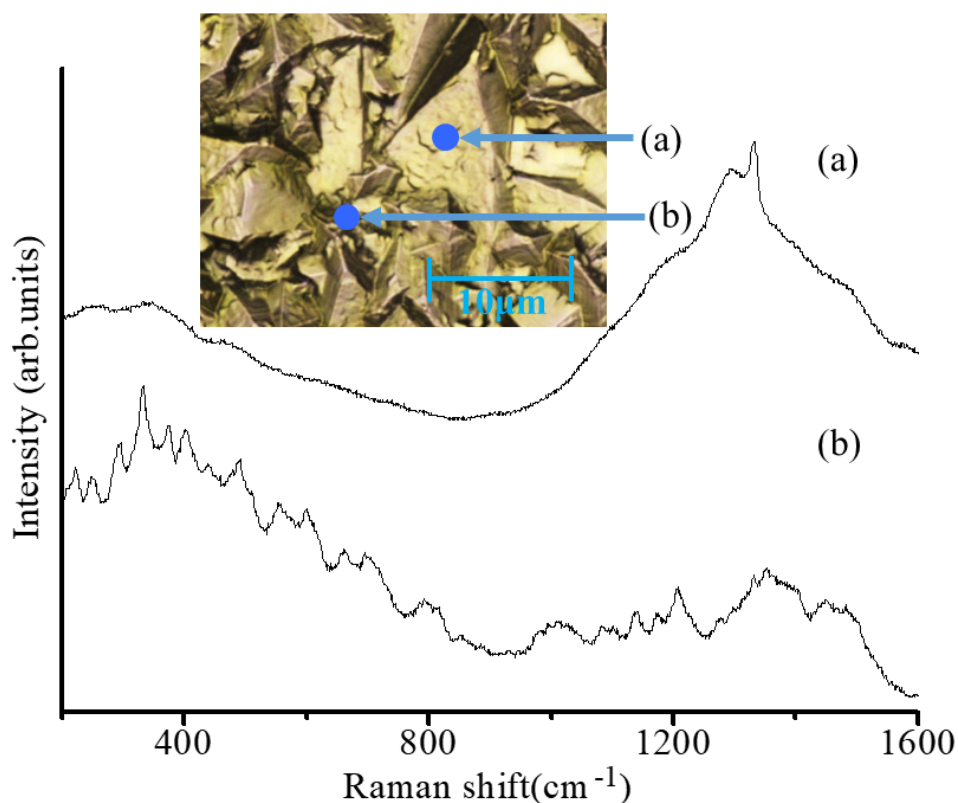


Figure 3-5. Raman spectra. (a) The area of the flat crystal surface. (b) The area containing grain boundaries. (Inset) The sampled area of bismuth doped sample by laser Raman microscope. (Diameter of laser spot is about 2  $\mu\text{m}$ ).

### 3.3.5 Distribution of Bismuth

The distribution of Bi in the sample was characterized by an isotope microscope (Fig. 3-6(a)). Carbon was uniformly distributed, while Bi was observed as spots. The distribution of Bi was similar to that of the grain boundaries (Fig. 3-6(b)). This indicates that the Bi had condensed between the grains of the diamond. The depth profile of bismuth was obtained by continuous SIMS-type operation of the isotope microscope. I carefully examined any periodicity in the depth profile, but the intensity of bismuth was constant. It suggests that the effect of the alternating bias

was concentrated in each grain boundary, not forming layers in the film. It is reasonable if I assume that the period of the alternating bias was shorter than the growth time of each crystalline grain.

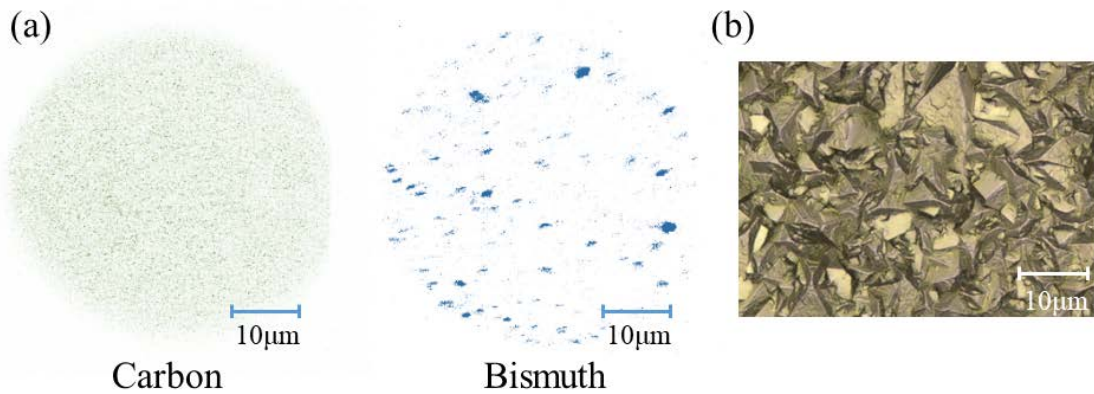


Figure 3-6. (a) Distributions of carbon and bismuth on the surface of the sample by using an isotope microscope. (b) Surface morphology of this sample by using a laser microscope.

### 3.3.6 Nanostructure of Films

Figure 3-7 shows the results of the TEM analysis. From samples (d-i), I observed two kinds of structures, *i.e.*, large grains (Fig. 3-7(a)) and nanoparticle aggregates (Fig. 3-7(b)). The diameter of the large grains and nanoparticles were 200 nm and 5–10 nm, respectively. It seems that the nanoparticles are covered with a thin wrapping (Fig. 3-7(b) inset). The large grains were identified as the diamond from the selected area electronic diffraction (SAED). The region of the nanoparticle aggregates showed SAED with rings and spots with a strong halo. The lattice

constants estimated from some of the rings and spots agreed with those of an unusual allotrope of carbon that is called Chaoite. Chaoite was first reported in meteorites [1,2], and it was also found as one of the byproducts during the diamond plasma CVD at the very early stages [33], laser photochemical etching [34], carbon liquid quenching [35], and electrochemical processes [36]. Although the structure of Chaoite has not been elucidated in detail, it is considered to contain a carbyne structure [1, 2], which can be very hard [3].

I observed bismuth from the EDS with the concentration of  $85 \pm 0.5\%$  in the area of nanoparticle aggregates. The area ratio of the core and shell, and the strong contrast in the core, strongly suggests that the core is made of bismuth and the shell is made of carbon. It should be noted that the nanostructures were only observed when the diamond growth occurred with bismuth immersion. The sample (d-ii) grown without the nucleation procedure did not contain nanoparticles. The sample (d-iii), which was formed by depositing Bi only, showed nothing on the Mo mesh. This indicates that large grains and nanoparticle aggregates were synthesized only in the condition with both the CH<sub>4</sub> and BEN processes. The source gas including Ar is not commonly used for the diamond thin film growth but used to synthesize an ultra-nanocrystalline diamond film [37]. When I used H<sub>2</sub> + CH<sub>4</sub> gas without Ar gas, the amounts of synthesized nanoparticle-aggregates were suppressed and the concentration of bismuth was low. In my growth conditions, the gas consisting of H<sub>2</sub>:Ar = 1:1 yielded polycrystalline the diamond and the nanoparticle aggregates at grain boundaries.

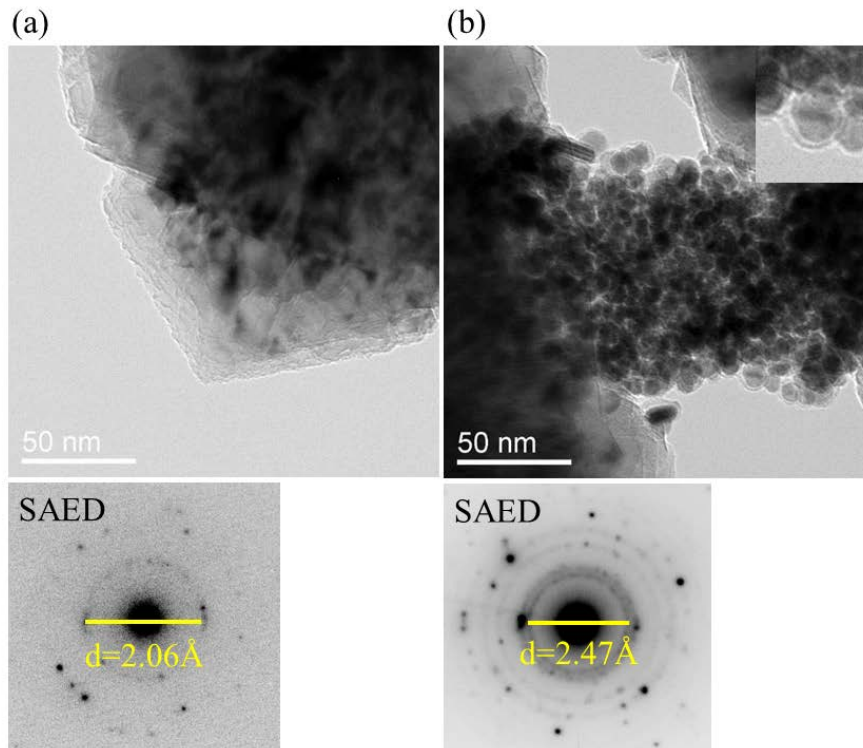


Figure 3-7. Results of the TEM analysis. (a) Large grains. (b) Nanoparticle aggregates.

### 3.3.7 Structure model

Figure 3-8 shows the presumed structure of a diamond film grown and Bi immersion with alternating bias. The sample is mainly composed of polycrystalline the diamond. There are nanoparticle aggregates at the grain boundary where Bi was only detected. The nanoparticles have core-shell structures. The shell probably contains molecule-like species such as diamondoids and bismuth-carbon clusters, as observed by the Raman microscopy (Fig. 3-5(b)). The core is composed of bismuth. There are also crystals of the unusual carbon allotrope Chaoite in this region. Since Bi-containing compounds show various useful functions such as photocatalysis [38–40] and multiferroics [41] partly in relation to the lone pair in the valence shell of

Bi, the Bi-C nanocomposite reported here may add a new variation in the functional Bi compounds and composites [42].

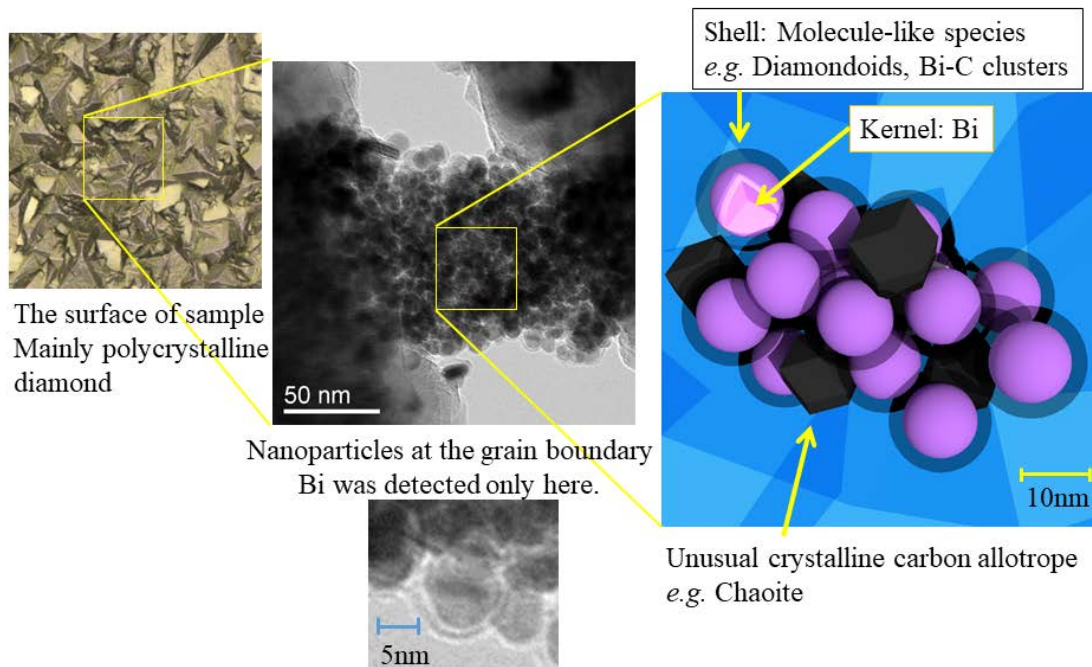


Figure 3-8. Presumed structure of the nanoparticle aggregates.

### 3.4 Conclusion

I investigated the possible doping of bismuth in the diamond by immersing bismuth in the plasma during the CVD growth of the diamond. The resulting film was polycrystalline the diamond showing an abnormal nucleation. The main portion of bismuth in the film was not in the diamond lattice, but it was included in the core of the aggregated nanoparticles at the grain boundaries. The shell of the nanoparticles contains molecule-like species such as the diamondoids or Bismuth-carbon clusters. I also detected the unusual carbon allotrope Chaoite near the grain boundary.

## References

- [1] A.G. Whittaker, P.L. Kintner, *Science* **165**, 589 (1969).
- [2] P.P. Smith, P.R. Buseck, *Science* **216**, 984 (1982).
- [3] M. Liu, V.I. Artyukhov, H. Lee, F. Xu, B.I. Yakobson, *ACS Nano* **7**, 10075 (2013).
- [4] W.L. Mao, H. K. Mao, P.J. Eng, T.P. Trainor, M. Newville, C. C. Kao, D.L. Heintz, J. Shu, Y. Meng, R.J. Hemley, *Science* **302**, 425 (2003).
- [5] Q. Li, Y. Ma, A.R. Oganov, H. Wang, H. Wang, Y. Xu, T. Cui, H.K. Mao, G. Zou, *Phys. Rev. Lett.* **102**, 175506 (2009).
- [6] K. Umemoto, R.M. Wentzcovitch, S. Saito, T. Miyake, *Phys. Rev. Lett.* **104**, 125504 (2010).
- [7] M. Amsler, J.A. Flores-Livas, L. Lehtovaara, F. Balima, S.A. Ghasemi, D. MacHon, S. Pailhès, A. Willand, D. Caliste, S. Botti, A. San Miguel, S. Goedecker, and M.A.L. Marques, *Phys. Rev. Lett.* **108**, 1 (2012).
- [8] A. Hiraiwa, H. Kawarada, *J. Appl. Phys.* **114**, 034506 (2013).
- [9] I. Aharonovich, A.D. Greentree, S. Praver, *Nat. Photonics* **5**, 397 (2011).
- [10] M.S. Grinolds, M. Warner, K. De Greve, Y. Dovzhenko, L. Thiel, R.L. Walsworth, S. Hong, P. Maletinsky, A. Yacoby, *Nat. Nanotechnol.* **9**, 279 (2014).
- [11] T. Iwasaki, F. Ishibashi, Y. Miyamoto, Y. Doi, S. Kobayashi, T. Miyazaki, K. Tehra, K.D. Jahnke, L.J. Rogers, B. Naydenzov, F. Jelezko, S. Yamasaki, S. Nagamachi, T. Inubushi, N. Mizuochi, M. Hatano, *Sci. Report.* **5**, 12882 (2015).
- [12] J.D. Hunn, N.R. Parikh, M.L. Swanson, R.A. Zuhr, *Diam. Relat. Mater.* **2**, 847 (1993).
- [13] J.L. DiMiglio, J. Rosenthal, *J. Am. Chem. Soc.* **135**, 8798 (2013).
- [14] K.E. Toghill, G.G. Wildgoose, A. Moshar, C. Mulcahy, R.G. Compton, *Electroanalysis* **20**, 1731 (2008).
- [15] K. Nakata, T. Ozaki, C. Terashima, A. Fujishima, Y. Einaga, *Angew. Chem. Int. Ed.* **53**, 871 (2014).
- [16] P.N. Volpe, J.C. Arnault, N. Tranchant, G. Chicot, J. Pernot, F. Jomard, P. Bergonzo, *Diam. Relat. Mater.* **22**, 136 (2012).
- [17] J.F. Prins, *Appl. Phys. Lett.* **41**, 950 (1982).
- [18] T. Tamura, T. Yanase, T. Nagahama, M. Wakeshima, Y. Hinatsu, T. Shimada, *Chem. Lett.* **43**, 1569 (2014).
- [19] A.V.M. Kunze, G. Dollinger, A. Bergmaier, E. Kohn, *Carbon* **37**, 787 (1999).

- [20] S. Yugo, T. Kanai, T. Kimura, T. Muto, *Appl. Phys. Lett.* **58**, 1036 (1991).
- [21] J. Nakata, Y. Hoshino, Y. Saito, K. Kawasaki, *Sci. J. Kanagawa University* **20**, 17 (2009).
- [22] NIST Atomic Spectra Database, <http://www.nist.gov/pml/data/asd.cfm2016> (accessed 16.06.16).
- [23] A.C. Ferrari, *Diam. Relat. Mater.* **11**, 1053 (2002).
- [24] H. Yurimoto, K. Nagashima, T. Kunihiro, *Appl. Surf. Sci.* **203-204**, 793 (2003).
- [25] B.E. Williams, J.T. Glass, *J. Mater. Res.* **4**, 373 (1989).
- [26] D. Saito, H. Isshiki, T. Kimura, *Diam. Relat. Mater.* **18**, 56 (2009).
- [27] J. Filik, J.N. Harvey, N.L. Allan, P.W. May, J.E.P. Dahl, S. Liu, R.M.K. Carlson, *Spectrochim. Acta A Mol. Biomol. Spectrosc.* **64**, 681 (2006).
- [28] P.W. May, J.a. Smith, K.N. Rosser, *Diam. Relat. Mater.* **17**, 199 (2008).
- [29] J. Filik, J.N. Harvey, N.L. Allan, P.W. May, J.E.P. Dahl, S. Liu, R.M.K. Carlson, *Phys. Rev. B* **74**, 035423 (2006).
- [30] J.E. Reddic, M.a. Duncan, *Chem. Phys. Lett.* **264**, 157 (1997).
- [31] Y. Yamada, T. Nakagawa, *Int. J. Mass Spectrom.* **282**, 123 (2009).
- [32] L. Gao, P. Li, H. Lu, S.F. Li, Z.X. Guo, *J. Chem. Phys.* **128**, 194304 (2008).
- [33] W. Yarbrough, R. Messier, *Science* **247**, 688 (1990).
- [34] J. Pola, A. Ouchi, S. Bakardjieva, V. Vorlicek, M. Marysko, J. Subrt, Z. Bastl, *J. Phys. Chem. C* **112**, 13281 (2008).
- [35] A.Y. Basharin, V.S. Dozhdikov, V.T. Dubinchuk, A.V. Kirillin, I.Y. Lysenko, M.A. Turchaninov, *Tech. Phys. Lett.* **35**, 428 (2009).
- [36] C. Pang, N. Li, C.X. Wang, *Electrochim. Acta* **141**, 226 (2014).
- [37] D.M. Gruen, *Annu. Rev. Mater. Sci.* **29**, 211 (1999).
- [38] A. Kudo, K. Omori, H. Kato, *Am. Chem. Soc.* **121**, 11459 (1999).
- [39] M. Shang, W. Wang, S. Sun, L. Zhou, L. Zhang, *J. Phys. Chem. C* **112**, 10407 (2008).
- [40] M. Guan, C. Xiao, J. Zhang, S. Fan, R. An, Q. Cheng, *J. Am. Chem. Soc.* **135**, 10411 (2013).
- [41] N.A. Hill, *J. Phys. Chem. B* **104**, 29, 6694 (2000).
- [42] G.-H. Hwang, S.-J. Hong, W.-K. Han, J.-S. Park, S.-G. Kang, *ECS Trans.* **16**, 557 (2008).

## Chapter 4 Surface Scientific Study of cBN

### 4.1 Introduction

The cBN has a similar crystal structure to that of the diamond. cBN is a very promising material that has high thermal conductivity, extreme hardness, and a large electronic bandgap. Its surface chemistry is expected to be different from that of the diamond. For example, the diamond easily reacts with iron whereas cBN does not, which makes cBN suitable for superhard coatings of cutting tools for iron-based materials. Plasma processes of cBN will become important because it is also a promising material in electronics, including for deep-UV LEDs[1], and power device applications[2,3].

Interfaces between cBN and the diamond and their mixed crystal are attracting much attention from the perspectives of both basic crystal engineering and applications[4]. The lattice mismatch between cBN and the diamond is rather small (1.4%) but the hardness of the crystal lattice of these materials makes lattice relaxation difficult. This leads to defects that act as carrier traps at the interfaces. The solution to this problem may be the formation of mixed crystals with a gradually changing composition or the preparation of surfaces with specific crystal indexes to form interfaces. In addition, there are many areas requiring physical study in the B–N–C alloy systems[5], because theoretical calculations predict various phenomena including spins and charge transfer complexes [6–8], which will exhibit spintronics [8] and photocatalysis[9]. From this viewpoint, reactions of cBN in plasma are very

important as well as the thin-film growth of highly crystalline cBN[10–16], because high-quality cBN films and their heterointerfaces with the diamond are mainly grown by plasma processes. A problem is that a technique for growing device-quality large single crystals of cBN has not been established in spite of considerable progress [17–26] and single crystal wafers are not available at present. I therefore started to study the plasma surface processes of cBN using very small single crystals grown by a HPHT technique, which are available as abrasive powder. I developed a method for handling the microscopic crystals and for preparing surfaces with different indexes. I studied plasma etching of cBN surfaces in  $H_2 + Ar$  and  $N_2$  plasmas, which are important for the growth of the diamond and cBN, respectively.

## **4.2 Experimental Section**

### **4.2.1 Handling of Small cBN Crystals and Their Surface Preparation**

I used octahedral cBN crystals with a typical diameter of 200  $\mu m$  (Global The diamond FBN300). In some of the experiments, I used crystals randomly fixed on a silicon wafer. Some of the crystals have well-developed faces with (111) and  $(\bar{1}\bar{1}\bar{1})$  surfaces, which are parallel to the silicon surface. The crystals were glued on a Si wafer with  $B_2O_3$  or an organic resin using a halogen lamp heater with a focusing parabolic mirror.  $B_2O_3$  has a melting point of 480  $^{\circ}C$  and a boiling point of 1680  $^{\circ}C$ . This high boiling point, which means a low vapor pressure, makes  $B_2O_3$  suitable for use in plasma processes and the high temperature environment of the diamond CVD. To obtain cBN surfaces with specific indexes, I glued a crystal on a glass capillary with an organic resin and set it on a four-axis X-ray diffractometer (Rigaku AFC 6).

Figure 4-1 shows photographs and a schematic drawing of the crystal alignment procedure using the four-axis diffractometer. The crystal was rotated to align the desired crystal axis perpendicular to the substrate surface. The Si wafer substrate ( $5 \times 2.5\text{mm}^2$ ) has a short and deep groove on one edge to fix the position of the crystal. After fixing the crystal with a small amount of organic glue,  $\text{B}_2\text{O}_3$  powder or a lamp of  $\text{B}_2\text{O}_3$  was placed near the crystal and heated by a lamp heater to melt and solidify the crystal. After the crystal axis alignment by using diffraction data, the crystal was fixed on a silicon wafer with  $\text{B}_2\text{O}_3$  keeping the specific angle. It was set in an ion beam cross-section polisher (CP; JEOL SM-09010) with the geometry shown in Fig. 4-2, and an ion beam with 6 kV acceleration voltage was collimated to 1 mm diameter and irradiated parallel to the surface plane of the silicon wafer for typically 12 h. A cBN surface parallel to the silicon wafer was obtained. I evaluated the crystal plane by electron backscatter diffraction (EBSD; JEOL JAMP-9500F). The crystal fixed on the silicon wafer was then introduced into the plasma process chamber (Fig. 4-2). Another Si wafer was placed to center the cBN crystal in terms of the plasma geometry.

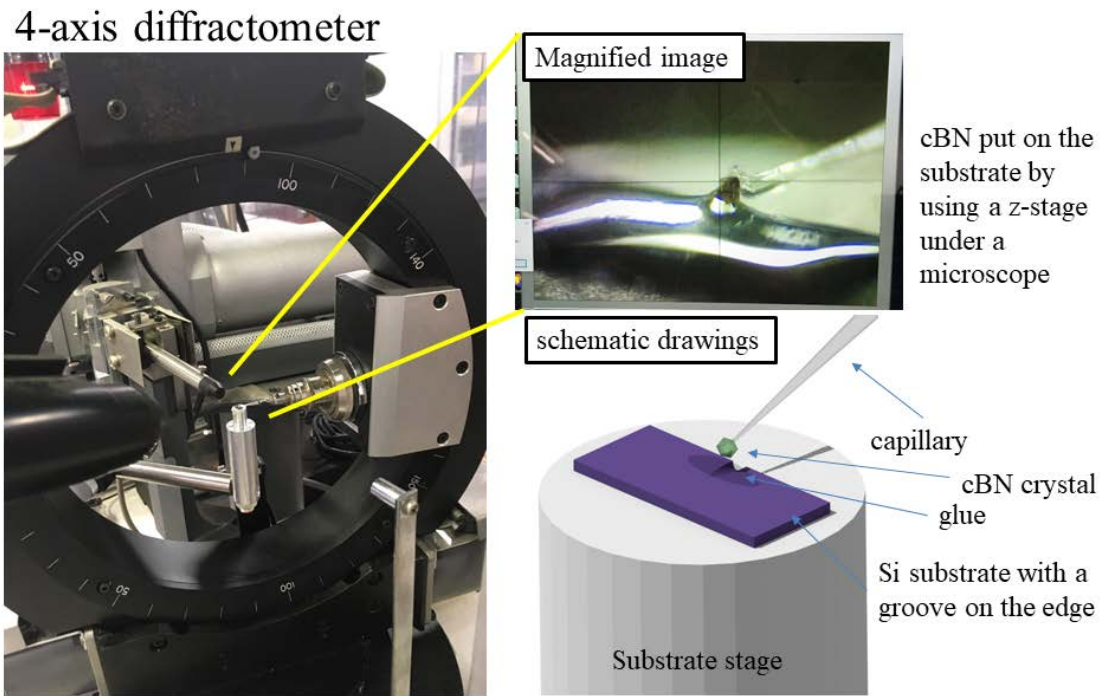


Figure 4-1. Procedure to align the crystal axis for ion beam CP. The bottom panels show the photographs taken during the fixation of a cBN crystal by melting  $B_2O_3$  without prior alignment by X-ray diffraction.

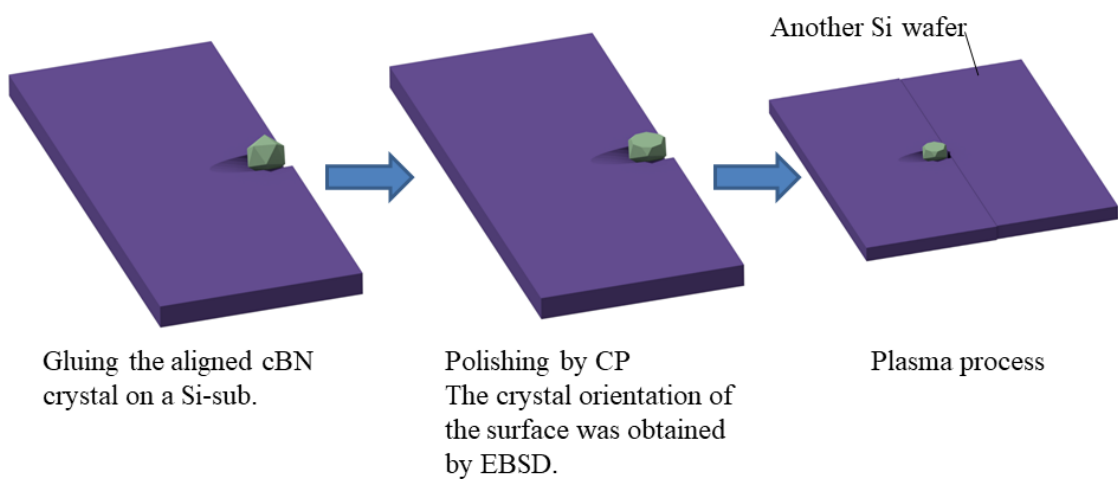


Figure 4-2. Sample geometry for the CP and plasma etching.

#### 4.2.2 Plasma Processes

I used compact microwave plasma CVD equipment that uses a microwave (2.45 GHz) antenna as the sample holder (ARIOS DCVD-51A-SSP) with laboratory-made modifications for doping and to optimize the design of sample holders [27, 28]. I introduced 80 sccm Ar–20 sccm H<sub>2</sub> mixed gas (purity 99.995%) or N<sub>2</sub> gas (80 sccm; purity 99.995%) to study the etching behavior in the plasma; these gasses are important for the plasma CVD growth of the diamond and cBN, respectively. The gas pressure was 6.0 kPa. The sample temperature was monitored with a pyrometer (Konica Minolta TR-630) through a quartz window and they were 950 and 900 °C for Ar–H<sub>2</sub> and N<sub>2</sub>, respectively. The spot size in the pyrometer measurement was  $\phi$  2mm, and near-infrared (NIR) radiation of 0.8–1.1  $\mu$ m wavelength was monitored with the emissivity value of 0.70 (calibrated for Si by the manufacturer). The microwave power heated the sample holder and there was no independent sample heater in the equipment. The temperature was mainly determined by the choice of the gas and was controlled to a lesser extent by tuning the microwave power (ca. 150W) to fix the temperature parameter in each experiment.

#### 4.2.3 Characterization

I used a laser microscope (Keyence VK-8710) to observe the surface morphology of the sample after the plasma etching. I used Raman microscopy (Renishaw inVia with 532 nm excitation) to characterize the material and the surface index of the cBN crystals. Since it was difficult to distinguish (111) and  $(\bar{1}\bar{1}\bar{1})$  surfaces by EBSD, Raman spectra were used complementarily.

## 4.3 Results and Discussion

### 4.3.1 Plasma Etching of cBN

First, I examined the etching behavior by changing the plasma gas. Figure 4-3 shows the laser optical microscopy images of cBN crystal (a) as purchased, (b) after Ar+H<sub>2</sub> plasma treatment for 24 h, and (c) after N<sub>2</sub> treatment for 24 h. One can clearly observe that a smooth surface was obtained after Ar+H<sub>2</sub> etching, whereas a rough surface appeared after N<sub>2</sub> etching. The etching rates were estimated by measuring the differences in the edge lengths of the crystals before and after the etching by laser microscopy to calculate the etching depth, and then dividing it by the etching time. They were 43 and 184 nm/h for Ar+H<sub>2</sub> and N<sub>2</sub>, respectively. Although the process temperature was higher for Ar+H<sub>2</sub> (950 °C vs 900 °C), the etching rate was lower in Ar+H<sub>2</sub>. It is clear that the etching speed is mainly determined by the chemistry in the plasma.



Figure 4-3. Laser optical microscopy images of a cBN crystal before and after plasma etching: (a) before etching, (b) after Ar+H<sub>2</sub> plasma etching, and (c) after N<sub>2</sub> plasma etching.

Next, I investigated the etching behavior of cBN {111} surfaces in N<sub>2</sub> plasma.

Figure 4-4 shows laser microscopy images taken (a) before and (b) after the N<sub>2</sub> plasma treatment. In Fig. 4-4(b), triangular etch pits, which can be clearly seen in the magnified image in Fig. 4-4(c), were observed on some faces of the cBN crystal after the N<sub>2</sub> plasma etching. However, neighboring faces do not show the triangular etch pits but a terrace-like morphology. This indicates that the plasma surface chemistry is dependent on the surface index. {111} surfaces of cBN are classified into (111) faces that have B atoms with one dangling bond per atom [(111)B] and ( $\bar{1}\bar{1}\bar{1}$ ) faces that have N atoms with one dangling bond per atom [ $(\bar{1}\bar{1}\bar{1})$ N]. Since it is difficult to determine the crystal surface indexes by EBSD, I obtained Raman spectra from a microscopic region of the cBN surfaces (Fig. 4-5). It has been reported that the intensity ratio of two strong peaks of cBN Raman spectra depends on the surface index ({111} and {100}) [29, 30]. Additionally, strong signals from defects at 925 and 955 cm<sup>-1</sup> are observed only from a ( $\bar{1}\bar{1}\bar{1}$ )N surface[29]. I concluded that the surface with triangular etch pits was a ( $\bar{1}\bar{1}\bar{1}$ )N surface, while that showing the terrace-like morphology was (111)B.

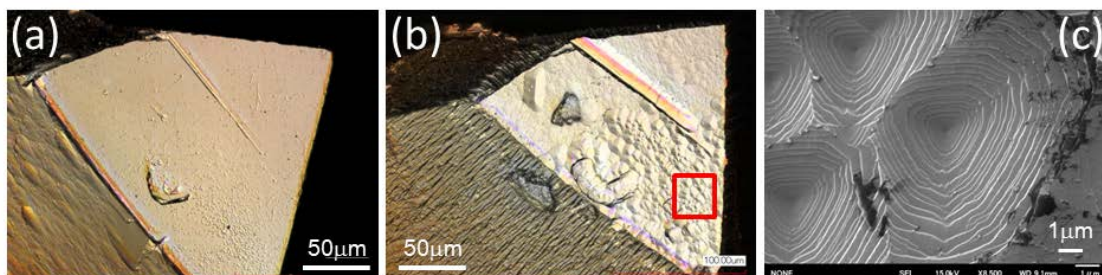


Figure 4-4. Microscopy images of a cBN crystal before and after N<sub>2</sub> plasma etching: (a) before etching (laser optical microscopy), (b) after N<sub>2</sub> plasma etching

showing the difference in the morphology between adjacent crystal faces (laser optical microscopy), and (c) magnified image of the region in (b) indicated by a square (scanning electron microscopy; SEM).

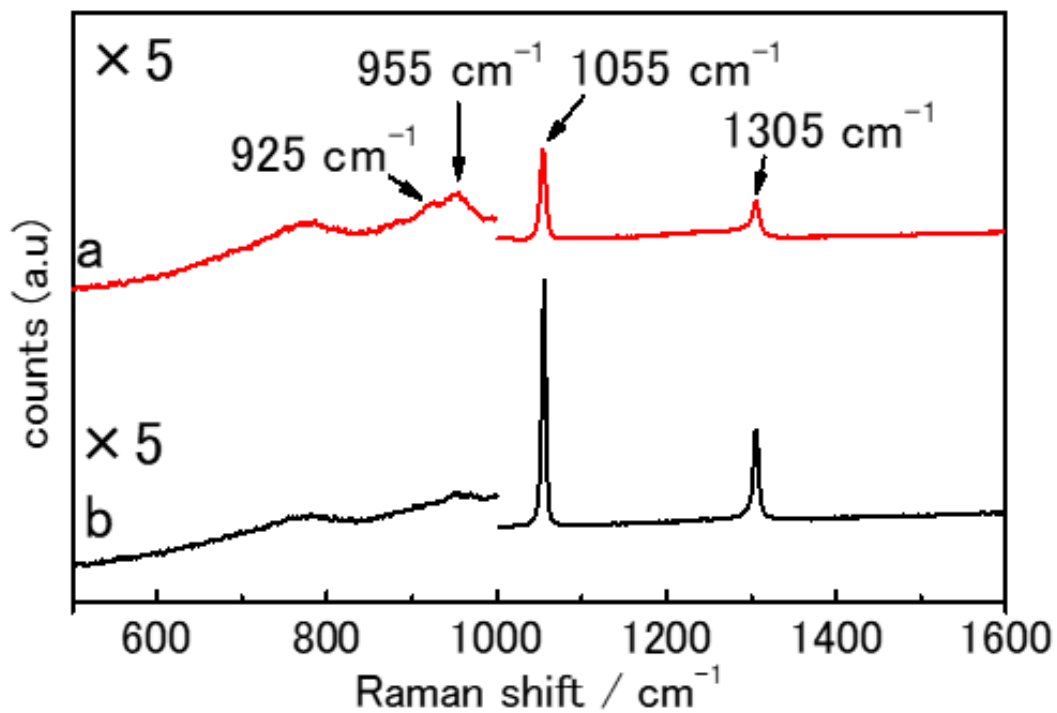


Figure 4-5. Raman spectra from the surfaces (a) with and (b) without triangular etch pits.

The mechanism resulting in this different etching is probably related to the electron occupancy of the dangling bonds between B and N atoms, as discussed to explain the selective growth of the diamond on cBN [31]. Figure 4-6 illustrates the mechanism. I make a reasonable assumption that the topmost surface is made of

atoms bonded with three atoms, which have one dangling bond per atom. On a  $(\bar{1}\bar{1}\bar{1})$ N surface, N atoms with a dangling bond and a lone pair of electrons make up the topmost surface. Since positive ions are the major species in plasma [32], positive ions of nitrogen containing atoms or molecules attack the lone pair to form  $N_2$  molecules that evaporate. On the other hand, B atoms with a vacant dangling bond make up the  $(111)$ B surface. Therefore, positive ions such as  $N^+$  cannot form volatile species with B because of the lack of bonding electrons. This accounts for the deep etching of  $(\bar{1}\bar{1}\bar{1})$ N surfaces. I consider that the appearance of triangular etch pits on  $(\bar{1}\bar{1}\bar{1})$ N is related to the crystal dislocations formed during the crystal growth of cBN crystals.

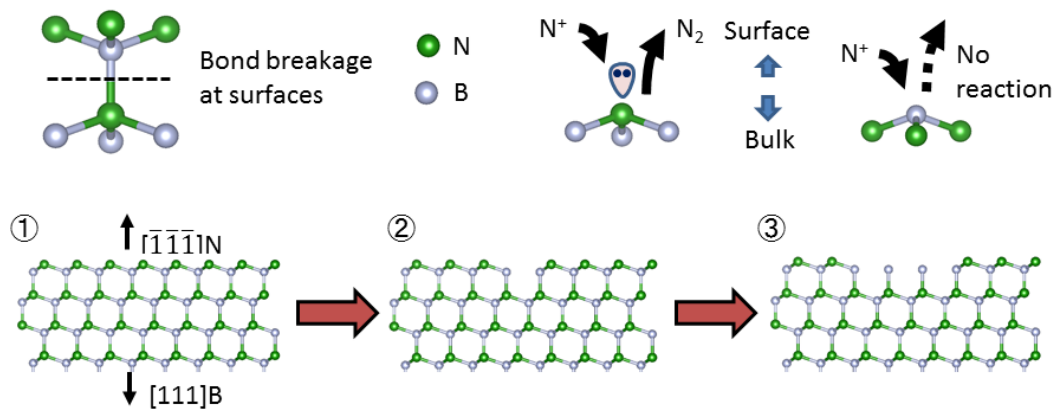


Figure 4-6. Illustration of the different plasma etching behaviors between  $(111)$ B and  $(\bar{1}\bar{1}\bar{1})$ N.

### 4.3.2 Plasma Etching of High-Index Surfaces

There have been some reports on the diamond growth by CVD on cBN microcrystals. However, they only used naturally available surfaces such as (111) and (001). High-index surfaces have not been studied. Therefore, I have developed techniques to prepare clean surfaces with arbitrary crystal indexes as described in the experimental section. Mechanical polishing is not a good choice because cBN is one of the hardest known materials. Also, the use of the diamond abrasive will result in the embedding of small the diamond particles into the surface. The CVD growth of the diamond is very sensitive to nucleation, and even the scratching of Si surfaces by the diamond markedly enhances the nucleation. Therefore, I use an ion beam process for the crystal face preparation. Figure 4-7 shows optical images before and after the treatment by CP using Ar<sup>+</sup> ion beam with an acceleration voltage of 6 kV and the sample current was 110 mA. After 12 h of irradiation, a very smooth surface was obtained. I demonstrated the etching of the high-index surfaces of cBN. Figure 4-8 shows laser optical microscopy and SEM images of {7 7 4} and {-3-1-41} surfaces before and after N<sub>2</sub> plasma etching. Before the etching [Figs. 4-8(a), (b), (e), and (f)], shiny mirror surfaces were observed. The roughness was smaller than the resolution of the laser microscope (10 nm). This means that macroscopic faceting was not observed after this CP process even with high-index surfaces. After the etching, the laser microscopy images show roughness [Figs. 4-8(c) and (g)], and a characteristic quasiperiodic morphology was observed by SEM [Figs. 4-8(d) and (h)]. The structures will be analyzed in the next section.

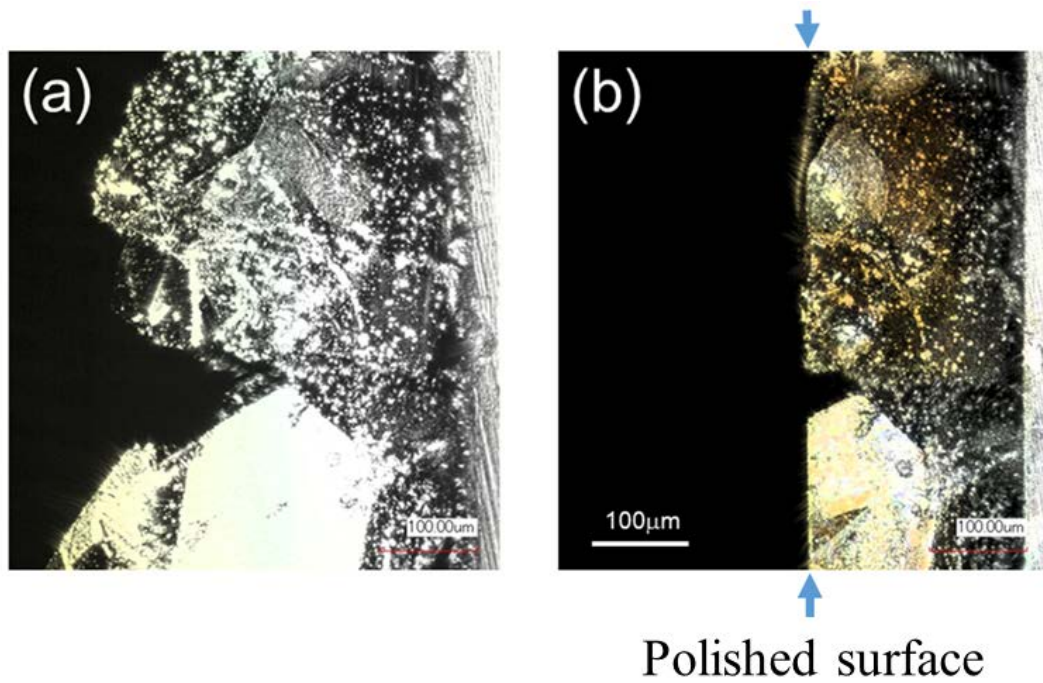


Figure 4-7. Preparation of flat surfaces by ion beam CP. Laser optical microscopy images (a) before CP and (b) after CP.

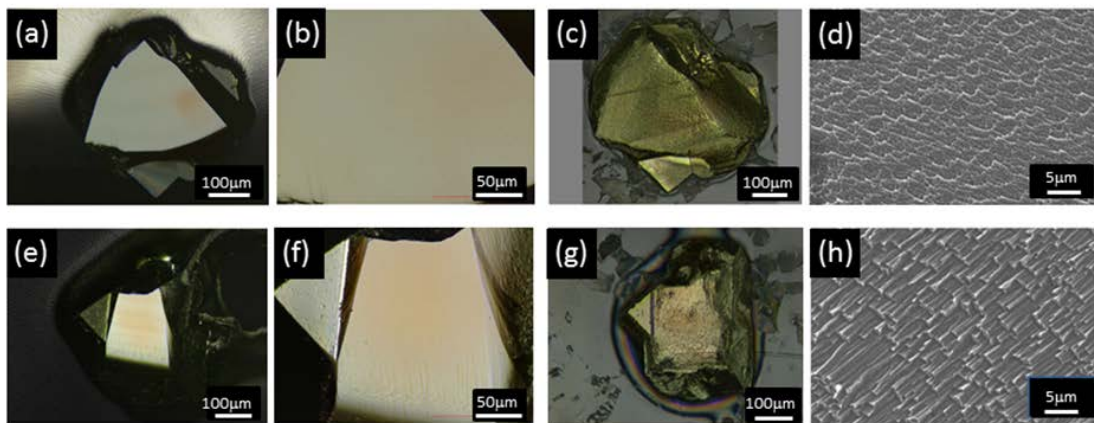


Figure 4-8. Microscopy images of cBN high-index surfaces before and after  $N_2$  plasma etching. (a)–(d)  $\{7\ 7\ 4\}$  surfaces and (e)–(g)  $\{-3\ -1\ -41\}$  surfaces. (a), (b), (e), (f) Laser microscopy images before the etching [(b), (d) magnified images].

(c), (g) Laser microscopy images after N<sub>2</sub> plasma etching. (d), (h) SEM images that show the characteristic morphology.

### 4.3.3 Atomistic Model of the Etching of High-Index Surfaces

In Sect. 4.3.1, I discussed the etching mechanism of cBN surfaces by the N<sub>2</sub> plasma. Here, I examine whether this mechanism can explain the observed periodic morphology of the high-index surfaces. Figure 4-9 shows an atomistic model of the high-index surfaces before and after the etching. Here, I assume that the (111)B surface is exposed after the etching because of the strong bonding of a topmost B atom to three N atoms underneath and because the positive charge of B atoms prevents the attack of positively charged nitrogen species in the plasma. Figure 4-9(a) illustrates the miscut (111)B surface before the etching of a  $\{7\ 7\ 4\}$  surface. After the etching, the (111)B facet forms the periodic structure shown in Fig. 4-9(b), which agrees well with the experimental observation [Fig. 4-8(d)]. Fig. 4-9(c) and (d) are illustrations of the  $\{-3\ -1\ -4\}$  surfaces (miscut  $\{0\ 0\ -1\}$ ). The miscut angle was chosen for the easily understandable illustration. The observed morphology [Fig. 4-8(h)] is also well reproduced in Figs. 4-9(d). Figures 4-9(e) and (f) show a similar model for a (111)B surface, which agrees well with the experiment [Fig. 4-4(c)]. These agreements support my hypothesis that the (111)B surface is resistant to N<sub>2</sub> plasma etching. The size of the quasi-periodic structure is due to faceting that exposes low-index surfaces, which have low surface energies. The kinetics of step and terrace evolution, or step bunching [33–35], is important for the surface nanostructuring.

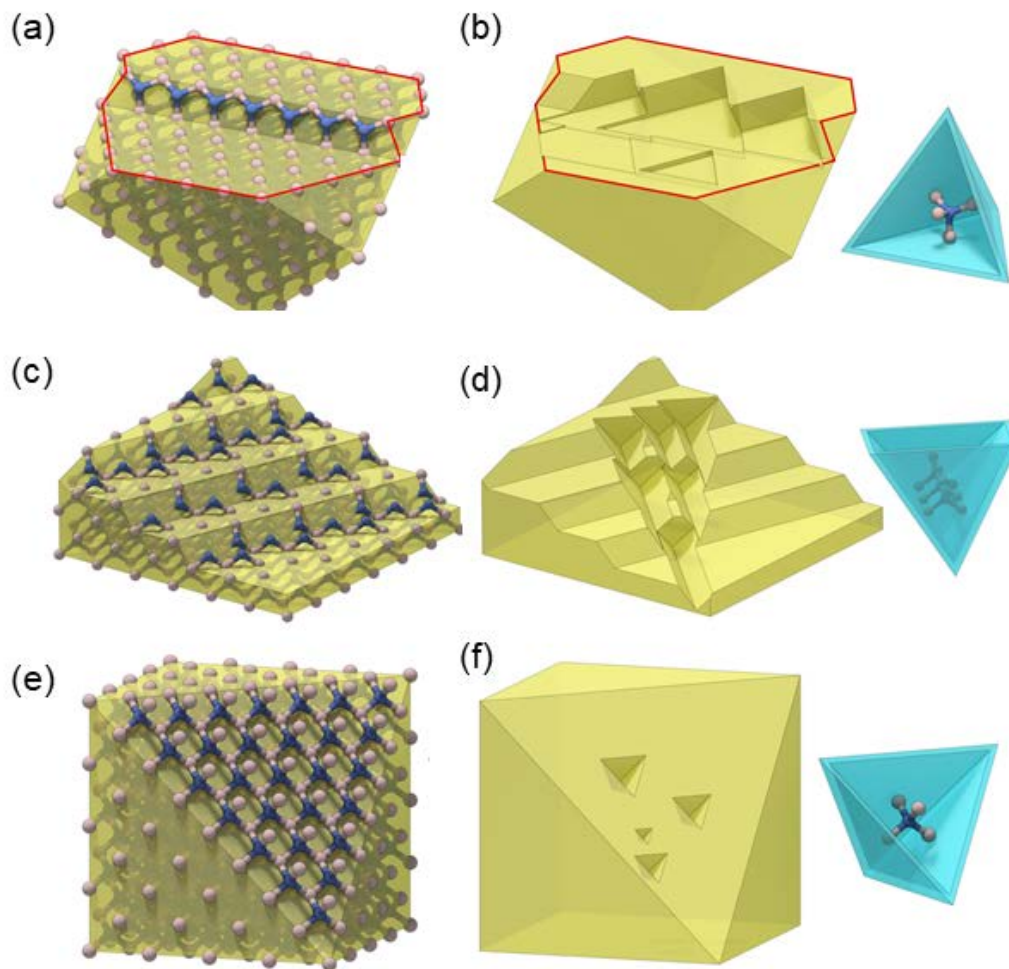


Figure 4-9. (Color online) Atomistic illustration of (a), (b)  $\{7\ 7\ 4\}$ , (c), (d)  $\{-3\ -1\ -41\}$ , and (e), (f)  $\{111\}$ , surfaces before (a), (c), (e) and after (b), (d), (f)  $N_2$  plasma etching.

#### 4.3.4 Etching with Solid $MgF_2$ inserted into Nitrogen Gas Plasma

In the previous section, I found the  $(\bar{1}\bar{1}\bar{1})N$  directional anisotropic etching effect of nitrogen plasma and clarified the etching mechanism. In establishing high quality gas phase synthesis, it is very important to investigate the effect of individual gas

species involved in the reaction on the crystal surface. Fluorine is an element often used in CVD synthesis of various solid crystals. Also in CVD of cBN, it has been reported that a reaction system containing fluorine in addition to B and N is effective for producing high quality cBN film [36]. However, the effect of fluorine plasma alone on the crystal surface in cBN growth is not well understood yet. In order to investigate this effect and make it a clue to establish a high-quality thin film synthesis method, I conducted experiments to confirm how much change is caused in the etching situation by adding a small amount of fluorine in nitrogen plasma.

The addition of fluorine into the nitrogen plasma was performed by inserting solid  $\text{MgF}_2$  as a raw material into the plasma and sputtering. The color of the plasma when  $\text{MgF}_2$  was inserted changed to a pale green color, [Fig. 4-10] and it was confirmed by analysis of the emission spectrum of this plasma that  $\text{MgF}_2$  became plasma. Plasma treatment was carried out for 24 hours by this method, and the change of crystal surface was examined using FE-SEM or laser microscope.

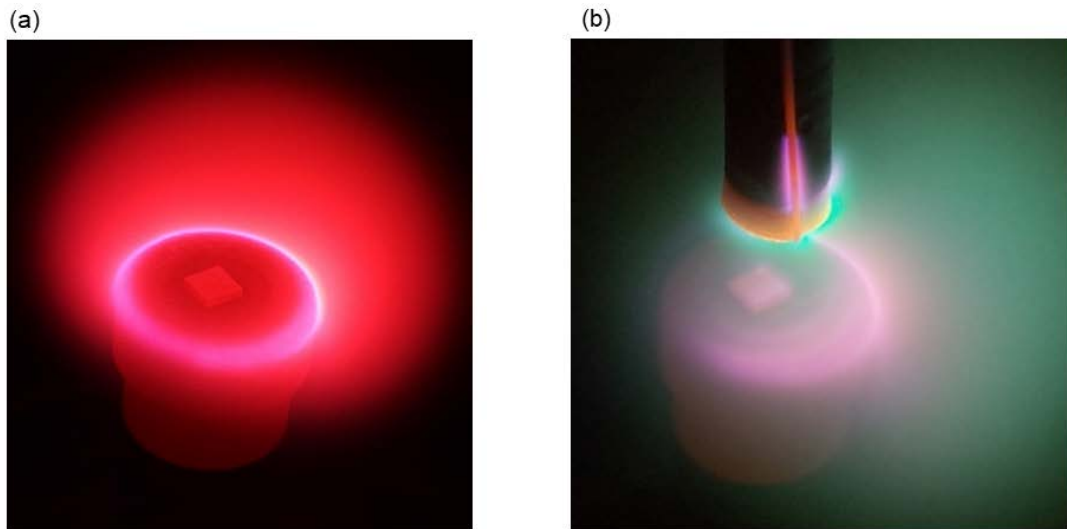


Figure 4-10. (a) Photograph of plasma during nitrogen etching. (b) Photograph when solid  $\text{MgF}_2$  is inserted into nitrogen plasma

Figure 4-11(a) shows the change of the crystal surface when plasma treatment is performed on the (111) plane. Unlike the case of etching with only nitrogen, triangular pyramidal protrusions are formed on the crystal surface. It can be seen that this protrusion is composed of three faces (100) (010) (001) by analogy from the positional relationship of the surrounding crystal planes. It is considered that this etching occurs probably because fluorine activated by microwaves reacts with nitrogen cations and so on to turn into nitrogen fluoride compounds such as  $\text{NF}_3$  and the etching effect of nitrogen decreases. The blue regular tetrahedron in Fig. 4-11(b-ii) is a conceptual diagram showing that the etching rate in the  $(\bar{1}\bar{1}\bar{1})\text{N}$  direction is fast. It is considered that the etching rate in the  $(\bar{1}\bar{1}\bar{1})\text{N}$  direction and the (110) direction decreases due to the introduction of fluorine anion and it changed from a

regular tetrahedron to a polyhedron in which apexes and edges of the regular tetrahedron as shown in Fig. 4-11(b-ii) were scraped. Such polyhedral etching occurs uniformly on the crystal surface due to fluorine introduction, and three surfaces of (100) are exposed as a stable surface other than the (111) B surface.

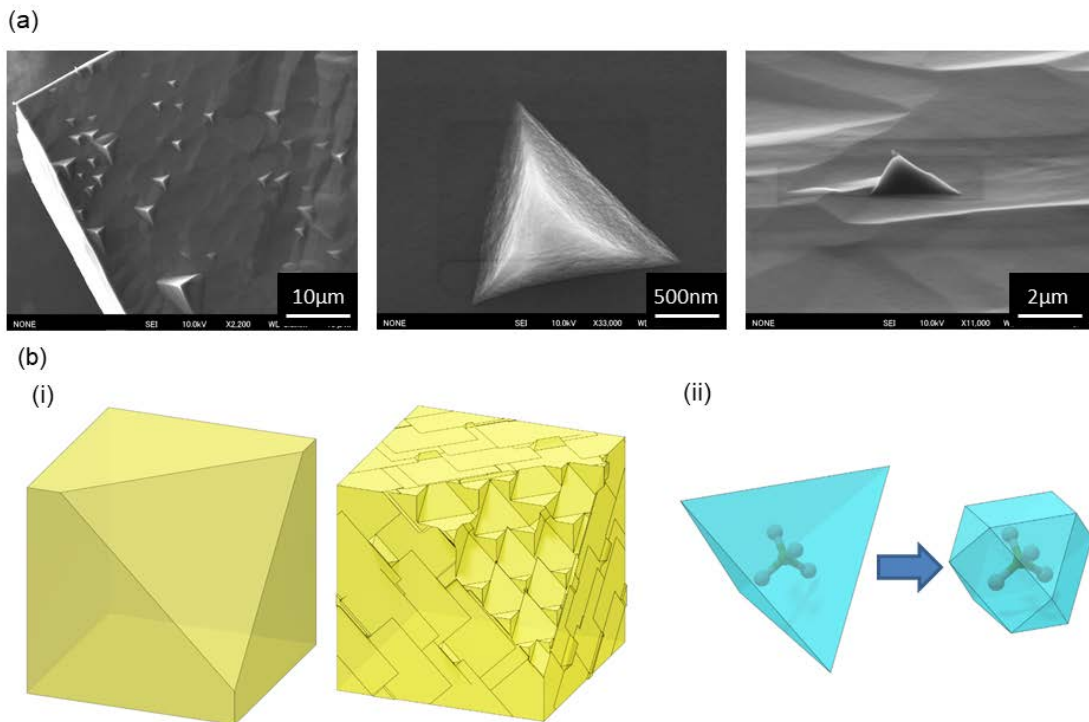


Figure 4-11. (a) FE-SEM image of crystal surface after  $N_2 + MgF_2$  plasma etching treatment. (b-i) Schematic diagram before and after etching of crystal surface. (b-ii) Change in etching rate relationship after addition of  $MgF_2$ .

The results of plasma treatment under the same conditions on the high index surface are shown in Fig. 4-12. Figure 4-12(a) is a laser microscopic image of the crystal surface after nitrogen etching. It can be seen that striped etching grooves are generated. The striped etching grooves suggest that this polished surface is a slightly

inclined surface from (100). Figure 4-12(b) is a crystal surface image after subsequently introducing  $\text{MgF}_2$ . It can be seen that a quasiperiodic structure of  $\mu\text{m}$  scale composed of three (100) planes was developed at a place where there was a crack compared with before etching.

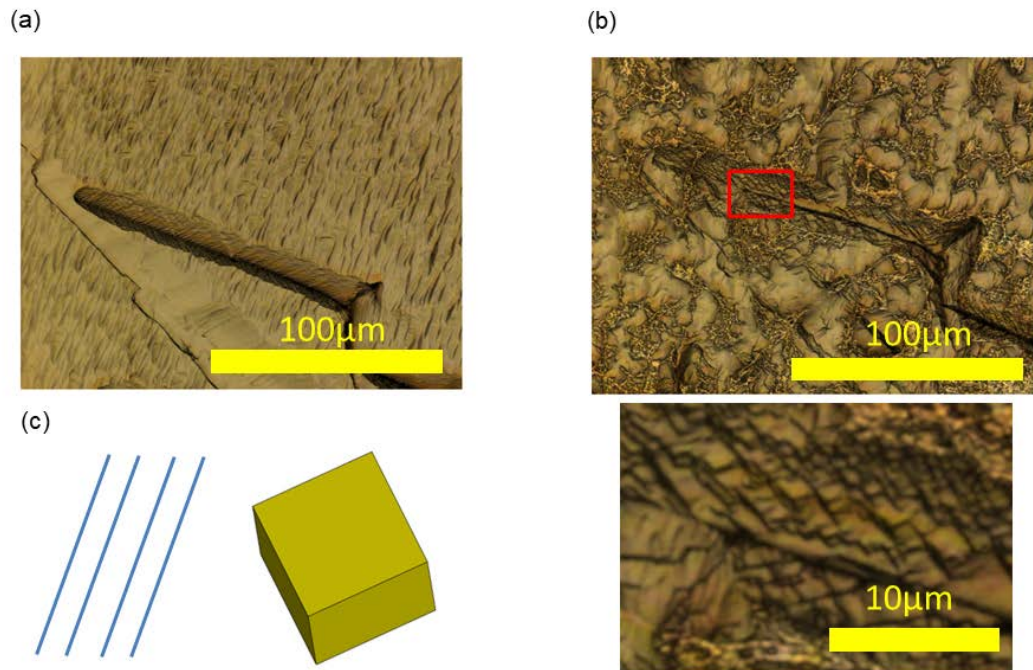


Figure 4-12. (a) Surface laser microscope image after nitrogen etching of high index surface. (b) Surface laser microscope image after  $\text{N}_2 + \text{MgF}_2$  plasma treatment. (c) Analogized crystal orientation. The striped pattern indicates the (110) direction.

From these results, it was found that introduction of  $\text{MgF}_2$  greatly affects the effect of nitrogen plasma etching.  $\text{MgF}_2$  reduces the etching effect in the  $(\bar{1}\bar{1}\bar{1})\text{N}$  and (110) directions due to nitrogen. By controlling the amount of  $\text{MgF}_2$  to be introduced,

it became possible to expose the (111) B surface and (100) surface by etching.

## 4.4 Conclusion

I developed a method for handling microscopic cBN crystals and studied N<sub>2</sub> plasma etching of the low- and high- index surfaces. Characteristic surface morphologies ranging from triangular etch pits to periodic faceting were observed. They can be explained by the stability of (111)B surfaces against the N<sub>2</sub> plasma etching, which originates from the strong three-directional bonding of positively charged topmost B atoms with N atoms.

It was also found that when MgF<sub>2</sub> was introduced into the nitrogen plasma, the effect of nitrogen plasma etching was greatly affected. MgF<sub>2</sub> reduced difference in the etching between the  $(\bar{1}\bar{1}\bar{1})$  N and (110) directions of nitrogen. By controlling the amount of MgF<sub>2</sub> to be introduced into the plasma, it became possible to expose the (111) B surface and (100) surface by etching.

## References

- [1] Q.-P. Dou, H.-T. Ma, G. Jia, Z.-G. Chen, K. Cao, C. Ren, J.-X. Zhao, X.-H. Liu, Y.-H. Zhang, and B. Shi, *Appl. Phys. Lett.* **88**, 154102 (2006).
- [2] K. Watanabe, T. Taniguchi, and H. Kanda, *Phys. Status Solidi* **201**, 2561 (2004).
- [3] X. W. Zhang, *Thin Solid Films* **544**, 2 (2013).
- [4] C. Chen, Z. Wang, T. Kato, N. Shibata, T. Taniguchi, and Y. Ikuhara, *Nat. Commun.* **6**, 6327 (2015).
- [5] L. Ci, L. Song, C. Jin, D. Jariwala, D. Wu, Y. Li, A. Srivastava, Z. F. Wang, K. Storr, and L. Balicas, *Nat. Mater.* **9**, 430 (2010).
- [6] A. K. Manna and S. K. Pati, *J. Phys. Chem. C* **115**, 10842 (2011).
- [7] W. Xie, T. Yanase, T. Nagahama, and T. Shimada, *Carbon* **2**, 2 (2016).
- [8] H. Park, A. Wadehra, J. W. Wilkins, and A. H. Castro Neto, *Appl. Phys. Lett.* **100**, 253115 (2012).
- [9] Y. Wang, X. Wang, and M. Antonietti, *Angew. Chem. Int. Ed.* **51**, 68 (2012).
- [10] A. Spiesser, Y. M. Chong, K. M. Leung, G. Abel, G. G. Ross, M. J. Walzak, R. Jacklin, W. M. Lau, W. J. Zhang, and I. Bello, *J. Phys. Chem. C* **111**, 12768 (2007).
- [11] Q. Li, Z. F. Zhou, C. S. Lee, S. T. Lee, and I. Bello, *Diam. Relat. Mater.* **10**, 1886 (2001).
- [12] S. Matsumoto and W. J. Zhang, *Diam. Relat. Mater.* **10**, 1868 (2001).
- [13] C. Y. Chan, W. J. Zhang, S. Matsumoto, I. Bello, and S. T. Lee, *J. Cryst. Growth* **247**, 438 (2003).
- [14] K. Hirama, Y. Taniyasu, S. Karimoto, Y. Krockenberger, and H. Yamamoto, *Appl. Phys. Lett.* **104**, 092113 (2014).
- [15] H. Yin, H.-G. Boyen, P. Ziemann, B. Dohuard, L. Houssiau, F. Renaux, M. Hecq, and C. Bittencourt, *Diam. Relat. Mater.* **17**, 276 (2008).
- [16] M. Noma, K. Eriguchi, Y. Takaho, N. Terayama, and K. Ono, *Jpn. J. Appl. Phys.* **53**, 03DB02 (2014).
- [17] S. K. Singhal and J. K. Park, *J. Cryst. Growth* **260**, 217 (2004).
- [18] S. K. Singhal, J. Von der Gonna, G. Nover, H. J. Meurer, and B. P. Singh, *Diam. Relat. Mater.* **14**, 1389 (2005).
- [19] O. Fukunaga, S. Takeuchi, and T. Taniguchi, *Diam. Relat. Mater.* **20**, 752 (2011).
- [20] S. Hu, J. Yang, W. Liu, Y. Dong, S. Cao, and J. Liu, *J. Solid State Chem.* **184**, 1598 (2011).

- [21] J. von der Gönna, H. J. Meurer, G. Nover, T. Peun, D. Schönbohm, and G. Will, *Mater. Lett.* **33**, 321 (1998).
- [22] O. Fukunaga, *Diam. Relat. Mater.* **9**, 7 (2000).
- [23] O. Fukunaga and S. Takeuchi, *Int. J. Refract. Met. Hard Mater.* **55**, 54 (2016).
- [24] R. H. Wentorf, *J. Chem. Phys.* **26**, 956 (1957).
- [25] T. Taniguchi, S. Koizumi, K. Watanabe, I. Sakaguchi, T. Sekiguchi, and S. Yamaoka, *Diam. Relat. Mater.* **12**, 1098 (2003).
- [26] Y. Kubota, K. Watanabe, and T. Taniguchi, *Jpn. J. Appl. Phys.* **46**, 311 (2007).
- [27] T. Tamura, T. Yanase, T. Nagahama, M. Wakeshima, Y. Hinatsu, and T. Shimada, *Chem. Lett.* **43**, 1569 (2014).
- [28] T. Tamura, T. Takami, S. Kobayashi, T. Nagahama, T. Yanase, and T. Shimada, *Diam. Relat. Mater.* **69**, 127 (2016).
- [29] S. Feng, L. Hou, X. Liu, Y. Gao, X. Li, Q. Wang, Z. Chen, G. Jia, and J. Zheng, *Appl. Surf. Sci.* **285**, 817 (2013).
- [30] W. J. Zhang, Y. M. Chong, I. Bello, and S. T. Lee, *J. Phys. D*, **40**, 6159 (2007).
- [31] S. Koizumi and T. Inuzuka, *J. Appl. Phys.* **32**, 3920 (1993).
- [32] J. Henriques, E. Tatarova, F. M. Dias, and C. M. Ferreira, *J. Phys.: Conf. Ser.* **516**, 012004 (2014).
- [33] J. L. Lin, D. Y. Petrovykh, J. Viernow, F. K. Men, D. J. Seo, and F. J. Himpsel, *J. Appl. Phys.* **84**, 255 (1998).
- [34] M. Ohtomo, T. Suzuki, T. Shimada, and T. Hasegawa, *Appl. Phys. Lett.* **95**, 123308 (2009).
- [35] T. Shimada, M. Ohtomo, T. Suzuki, T. Hasegawa, K. Ueno, S. Ikeda, K. Saiki, M. Sasaki, and K. Inaba, *Appl. Phys. Lett.* **93**, 223303 (2008).
- [36] W.J. Zhang and S. Matsumoto, *Chem. Phys. Lett.* **330**, 243 (2000).

# **Chapter 5 Mechanical Properties of Various Index Planes of cBN from Nanoindentation**

## **5.1 Introduction**

### **5.1.1 Importance of Elucidating the Mechanical Properties of cBN**

In the previous chapter, I mentioned experiments to investigate the plasma etching effect of various gas as the first step for gas phase synthesis of cBN.

Establishment of high quality gas phase synthesis method is an important issue to be solved in device application, but it is also an important issue in basic research. Studies on the basic physical properties and chemical properties of single crystal cBN have been impossible because high quality gas phase synthesis method is difficult and large area crystals cannot be obtained. Sintered bodies and polycrystalline thin films were only used until now. The semiconductor and fundamental properties of single crystal cBN have not yet been clarified.

The mechanical properties of single crystals are factors that greatly affect performance in the design of cutting tools, semiconductor devices and micro electron mechanical systems (MEMS). These properties are strongly related with the generation, multiplication, and motion of dislocations, which must be studied using nano-probe under motion. Nanoindentation is the technique suitable for that purpose. The result of the nanoindentation can be related with the macroscopic mechanical properties. Hardness and Young's modulus reflect resistance to plastic and elastic

deformation, respectively.

In this chapter, experiments were conducted to investigate the mechanical properties which are fundamental physical properties by using cBN single crystal grains. cBN single crystal grains were polished and nanoindentation tests were performed on various index surfaces. The nanoindentation is an experiment that can investigate nanoscale hardness and elastic modulus, crystal phase transition, dislocation, etc. of a substance by pressing a nano-sized the diamond probe against the material surface.

### **5.1.2 Problems in Nanoindentation of cBN**

Nanoindentation test using micro cBN single crystal has two technical problems (Fig. 5-1). The first problem is fixation of samples. It has been reported from the nanoindentation test results of sintered bodies and vapor deposited thin films that cBN has hardness and modulus comparable to that of the diamond.

Since it is such a hard material, it is necessary to apply a very high pressure when testing a single cBN crystal grain by nanoindentation. However, since the crystal of cBN is about 300  $\mu\text{m}$ , extremely high pressure is applied to the part supporting the crystal. Since the adhesive used for fixing the crystal and the sample support are subject to the high pressure that causes their crush and deformation, accurate measurement cannot be performed. It is therefore necessary to develop a method to fix the sample onto a very hard support material without using adhesives. The second problem is that it is necessary to create a parallel and flat surface to prevent lateral

shift of the tip of the indenter probe. However, this processing is also difficult due to the very hard and small sample.

Regarding the first problem, the solution is explained in detail in Section 5.2.2 (sample fixing method and general indentation condition). The second one is explained in detail in 5.2.1 (sample preparation).

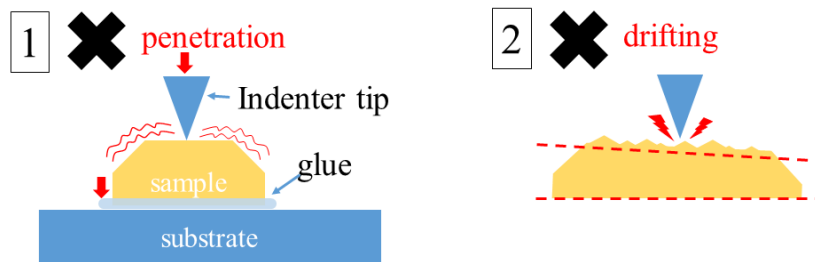


Figure 5-1. Problems to be solved for nanoindentation of the cBN

## 5.2 Experimental Section

### 5.2.1 Sample Preparation

The cBN used for the measurement is a particle synthesized by the HPHT method, which is a truncated tetrahedron with a corner of about 200  $\mu\text{m}$  in grain shape. (Global The diamond FBN 300). After burying a whole grain in ultraviolet curing resin (Technobit), defoaming treatment was carried out in a vacuum desiccator. Thereafter, UV light was irradiated for 30 minutes to cure the resin. In this way, it is possible to fix many crystal grains on the same plane (Fig. 5-2(a)). By carrying out planar polishing with a diamond grinding stone or SiC sandpaper, it is possible to fabricate a large number of plate-like cBNs with parallel random

orientation planes at once (Fig. 5-2(b)).

It was confirmed by indenter probe scan (SPM) and FE-SEM that the flatness of the crystal surface was 10 nm or better (Fig. 5-2(c)). Crystallographic index of the surface was acquired by FE-SEM-EBSD (Electron beam back scattered diffraction).

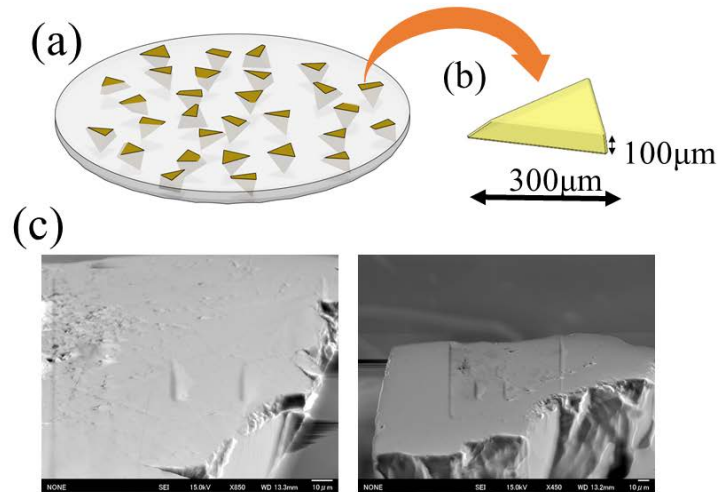


Figure 5-2. (a) Package of cBN crystal grains in resin. (b) cBN crystal plate after polishing on both sides. (c) FE-SEM image of polished cBN surface

### 5.2.2 Sample Fixing Method

The equipment used in this experiment was triboindenter manufactured by Hysitron Company. The indenter chip used in the experiment was spherical with a tip diameter of about 0.5 μm. The spherical tip is less susceptible to cracking when a load is applied, and the change of elastic deformation / plastic deformation of the sample can be measured. It is also often used for comparison with molecular dynamics simulation. The calibration of the indenter tip was performed using a reference sample of fused quartz. The hardness and elastic modulus measured in the

nanindentation were defined by ISO 14577.

In order to fix the sample crystal plate on the stage without using the adhesive, the equipment as shown in the Fig. 5-3(a) was used. cBN was placed on a sapphire substrate (1 cm square, 0.5 mm thick), the diamond substrate (2.5 mm × 0.5 mm thick) and surrounded with a rubber O ring (diameter 2 cm, rubber thickness about 1.2 mm), a 50 μm-thick tungsten sheet) covers the whole. A hole of about 100 μm is opened in the tungsten film. The tungsten holes are placed to overlap cBN as seen from above. As shown in the cross section (Fig. 5-3(b)), the sample was pressed against the tungsten film from above by the force of vacuum. Using this technique, cBN can be fixed to the measurement stage without using adhesive. The indenter tip can contact the sample surface through the hole of the tungsten sheet.

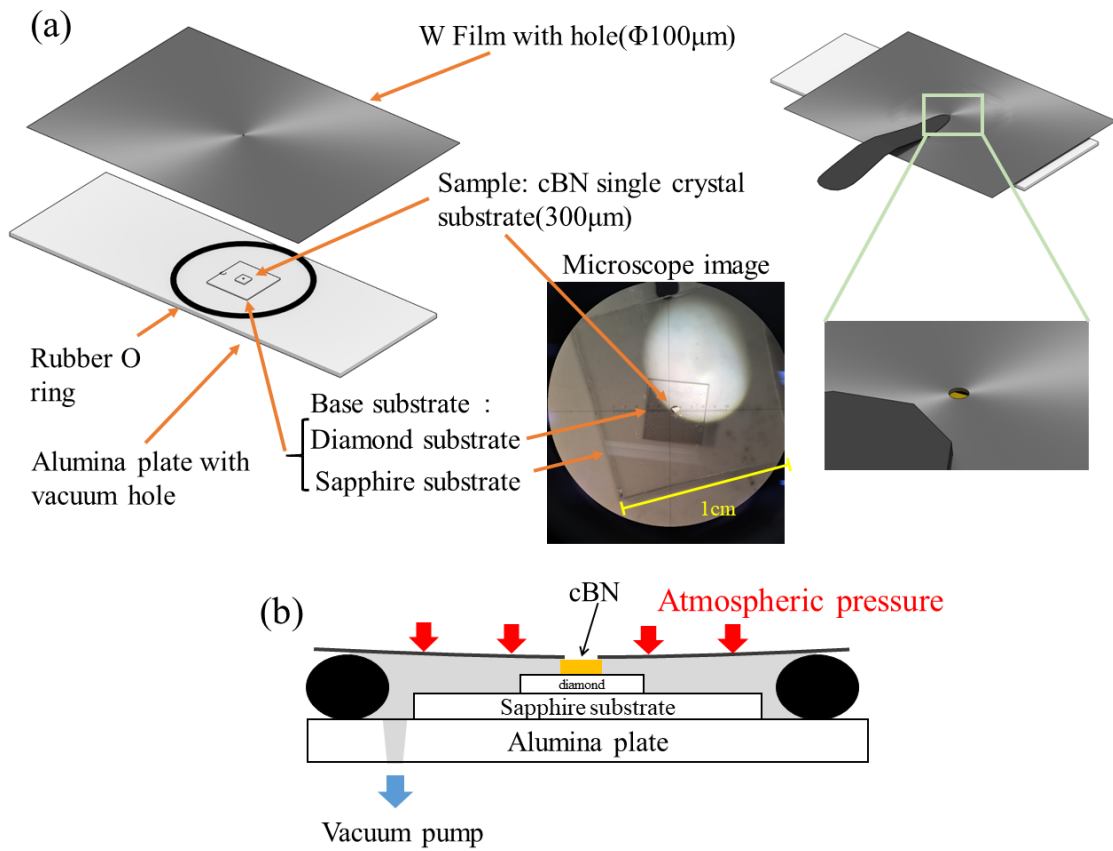


Figure 5-3. (a) Schematic diagram of cBN fixing system. (b) Schematic cross section.

Figure 5-4 shows the load condition of the indentation. First, the load was ramped to a target value in 5 s, then it was hold constant for 1 s, then it was ramped down in 5 s. the drift of the indenter tip was confirmed to be negligible by holding the indenter tip for 1 s on the sample surface.

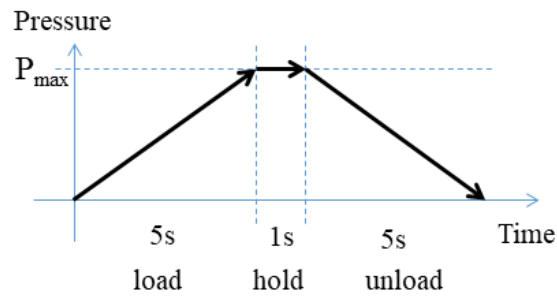


Figure 5-4. General load condition of indentation.

### 5.2.3 Indentation Condition

Two types of experiments were planned and successfully conducted. The first type was investigation of mechanical properties on variously indexed surfaces. 15 specimens with various surfaces was tested 11 points each at a time with 1000  $\mu\text{N}$  incremental target load (up to 12000  $\mu\text{N}$ ). From the indenter probe image, the place to be tested was selected as a place where it is found that the surface flatness was excellent. In this way, drift of the probe on the sample surface was suppressed. The second type of experiment was the analysis of mechanical properties near the twin interface of cBN single crystal. The region ( $50 \times 50 \mu\text{m}$ ) found to be twin in EBSD was divided into  $8 \times 8$  meshes, and a total of 64 points were measured under the same load condition. The maximum load was set to 10000  $\mu\text{N}$ .

## 5.3 Results and Discussions

### 5.3.1 Nanoscale Elastic Modulus and Hardness

A typical load application curve is shown in Fig. 5-5(a). This sample was found to be oriented almost to the (111) plane by characterization with EBSD. This surface was scanned with SPM, and the test was carried out at eleven points where it was found that the flatness was confirmed from the SPM image (Fig. 5-5(b)). After the all nanoindentation experiment, the samples were analyzed by AFM. The average surface roughness of a crystal surface was 0.66 nm. This value is sufficiently smaller than the size of indentation mark (about 500 nm) (Fig. 5-6). The elastic modulus and hardness at each measurement point are shown in Tab. 5-1.

Table 5-1. The elastic modulus and hardness at each measurement point.

$P_{max}$ ( $\mu\text{N}$ )	$E$ (GPa)	$H$ (GPa)	$h_{max}$ (nm)
1000	485.3	60.50	21.13
2100	659.1	177.3	36.21
3200	611.8	167.1	49.45
4300	452.3	84.00	75.94
5400	453.9	96.19	85.36
6500	457.6	103.4	95.57
7600	440.4	99.95	110.1
8700	442.3	103.5	120.3
9800	429.2	103.4	133.2
10900	420.8	103.2	145.8
12000	414.4	104.2	156.9
Mean/STD(GPa)	$478.8 \pm 80.5$	$109.3 \pm 33.4$	

When the maximum load was less than or equal to  $3000\mu\text{N}$ , the load application curve showed elastic deformation behavior, and when more than  $3000\mu\text{N}$  was applied, it showed plastic deformation behavior. The average hardness and elastic

modulus in the elastic deformation region were  $172.2 \pm 7.2$  GPa and  $635.4 \pm 33.5$  GPa, and in the plastic deformation region, it were  $99.7 \pm 6.0$  GPa and  $438.9 \pm 16.0$  GPa.

Hardness was calculated by dividing the pressure by the contact area of the indenter tip. In the elastic deformation region, the hardness showed a very high value. This value seems to be largely deviated because it is difficult to calculate the contact area when the load is low. The calibration of the contact area of the indenter tip was performed using a fused quartz sample as a reference, but since the measured sample was very hard, it is considered that the value of the contact area at the time of applying a low load largely deviates.

Recently, a nanoindentation experiment of the (111) face of the single crystal cBN was reported by using Berkovich type probe [1]. Table 5-2 shows the comparison of present results with previous reports including poly-crystalline samples [2-9]. By comparison, my samples were found to have low elastic modulus.

There are several factors that influence the differences in the hardness. The first is the different the shape of the probes. The second is the difference of concentration of impurities. Reference [1] has analyzed the impurities of the sample was less than 0.06%. The third is the difference in crystallinity. It is noted that the nanoindentation experiment of cBN has just started. I expect that my results will stimulate the research activities in this field.

As for the hardness of the plastic deformation region, I observed a value comparable to that of the diamond single crystal ( $\sim 100$  GPa [10]).

Table 5-2. Reported hardness (H) and Young's modulus (E) for c-BN determined from experiments and calculations. NI, V, and K indicate nanoindentation, Vickers, and Knoop hardnesses, respectively. B and D indicate Brillouin scattering and dynamic resonance measurements, respectively.

Ref.	$H(\text{GPa})$	$E(\text{GPa})$	Exp. or calc.	Crystal
This study	$90 \pm 10(\text{NI})$	$362 \pm 69$	Exp.	Single
1	$61 \pm 1(\text{NI})$	$1070 \pm 30$	Exp.	Single(111)
	$59 \pm 1(\text{NI})$	$960 \pm 30$	Exp.	Sintered
2	28.8-52.2(V)		Exp.	Sintered
3	49(V)		Exp.	Sintered
4	$63 \pm 5(\text{V})$		Exp.	No data
5	$\approx 60(\text{V})$		Exp.	Sintered
6	45(K)			
		998(B)	Exp.	Single(111)
7		665-894(D)	Exp.	Sintered
8		909	Calc.	-
		1049	Calc.	-
9		1023	Calc.	-

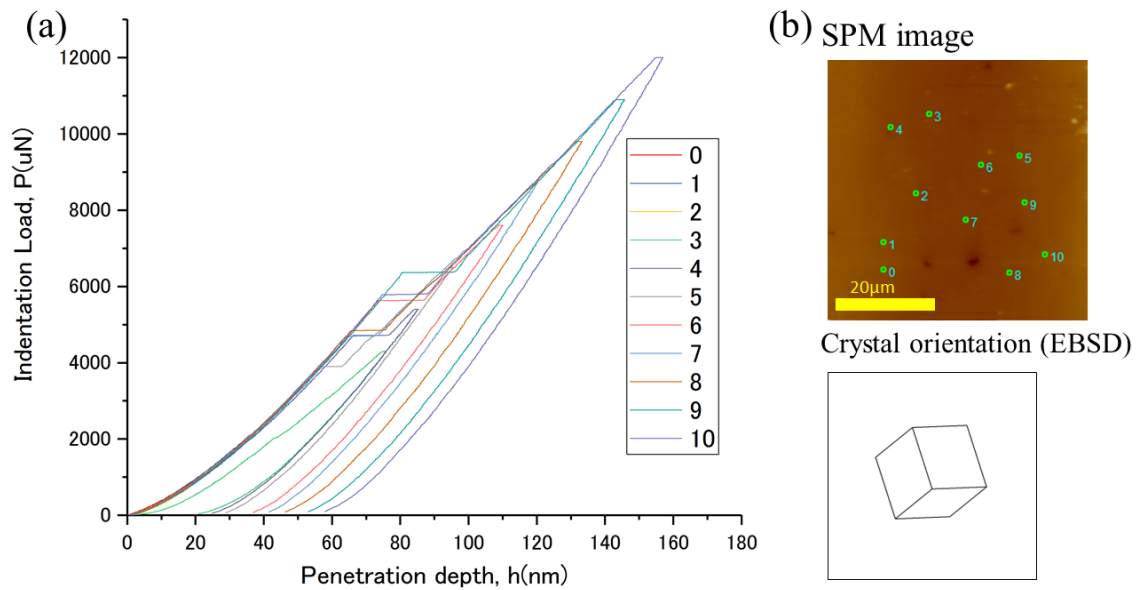


Figure 5-5. (a) Typical load application curve. (b) SPM image of sample surface and crystal orientation obtained from EBSD

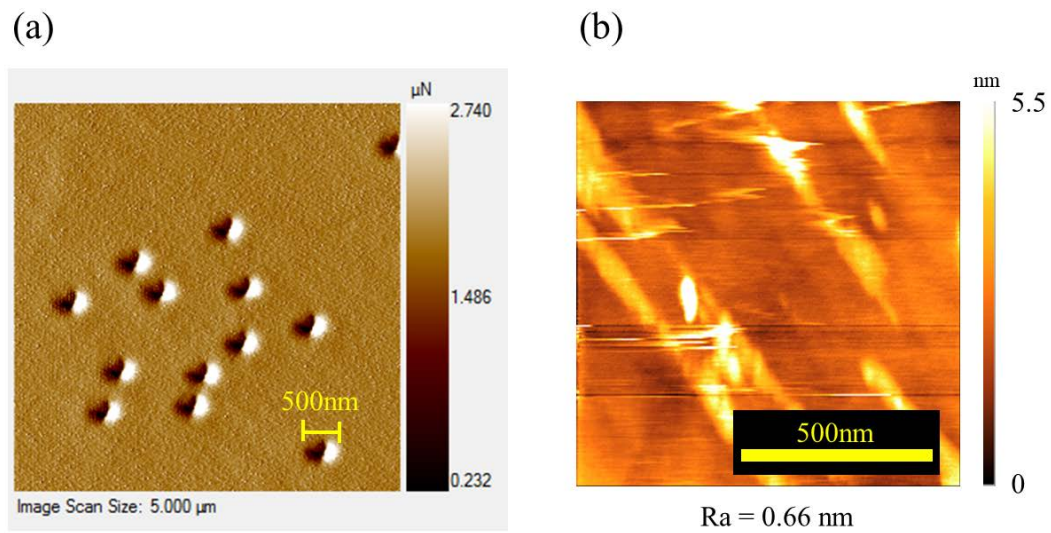


Figure 5-6. (a) Typical SPM image after indentation. (b) Typical AFM image of the polished crystal surface.

### 5.3.2 Pop-in

As can be seen from Fig. 5-5, it was found that the phenomenon called "pop-in" in which the probe suddenly sinks under a load of over a certain level (3900  $\mu\text{N}$  or more) occurs. Observation of the pop-in phenomenon in cBN single crystals has not been reported to the best of my knowledge. The pressure at which this pop-in phenomenon occurred was found to be  $58.1 \pm 3.1$  GPa from the contact area.

The pop-in phenomenon is generally thought to occur by irreversible collapse of atomic bonds (dislocation) or by phase transition. Figure 5-7 is a phase diagram showing the high pressure and high temperature phase of BN [11]. The possibility of the phase transition is excluded because cBN is a stable phase between 1.2 and 50 GPa and no phase transition to a denser phase is known from experiments [11] and calculation [12]. The other possible mechanism for the pop-in is dislocation. The dislocation of cBN tends to occur as slip dislocation along the (111) plane as elucidated from molecular dynamics simulation [12]. Therefore, it is considered that these dislocations are generated during load application. There were variations in the timing of the pop-in start, which is thought to be caused by slightly different conditions such as impurities and defect distribution near the tested point.

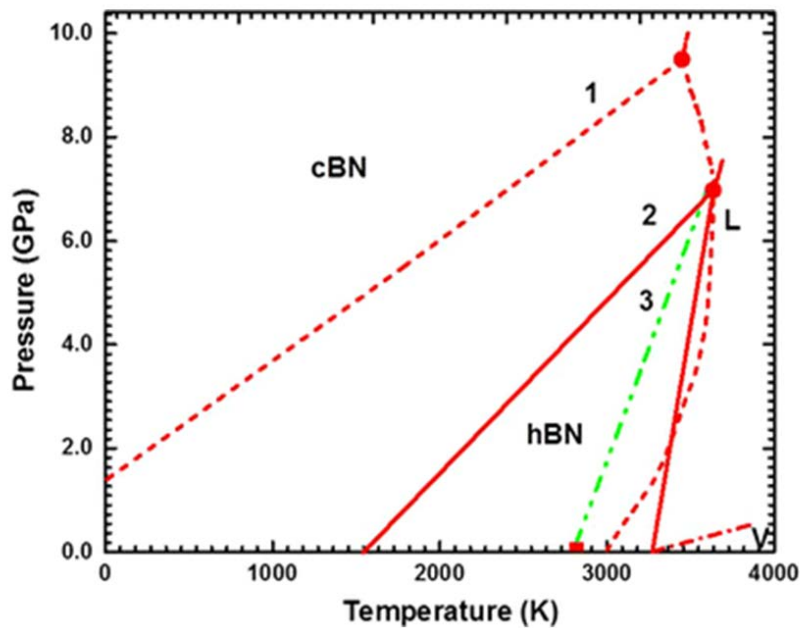


Figure 5-7 Phase diagram of boron nitride [11].

### 5.3.3 Surface Orientation Dependence of Mechanical Properties

In this experiment, the samples were randomly oriented before polished. For the analysis, they were tentatively classified into three low indexed faces, *i.e.*, (111), (100) and (110). This treatment is justified because the probe has the spherical (or conical) shape in the nanoindentation experiment and slight difference in the angles were absorbed into the probe shape factor. The crystallographic index of the sample surfaces were analyzed by EBSD. The angles from the surface normal and the  $\langle 111 \rangle$ ,  $\langle 100 \rangle$  and  $\langle 110 \rangle$  vectors were calculated from their inner products. The surfaces were classified to the planes giving smallest angles. Figure 5-8 shows the hardness and elasticity modulus of 15 specimens. The average deviation of the orientation was shown in the caption of Fig. 5-8.

It clearly proved that the (100) direction is the hardest. It is consistent with the result of theoretical calculation that it is difficult to generate (111) slip dislocation in the (100) plane. The value of the (110) plane was particularly low. This agrees with theoretical calculation result that (111) slip dislocation tends to spread in this direction.

The elastic modulus showed the same tendency as hardness.

From the above, it was found that both hardness and elastic modulus are high in the order of (100), (111) and (110).

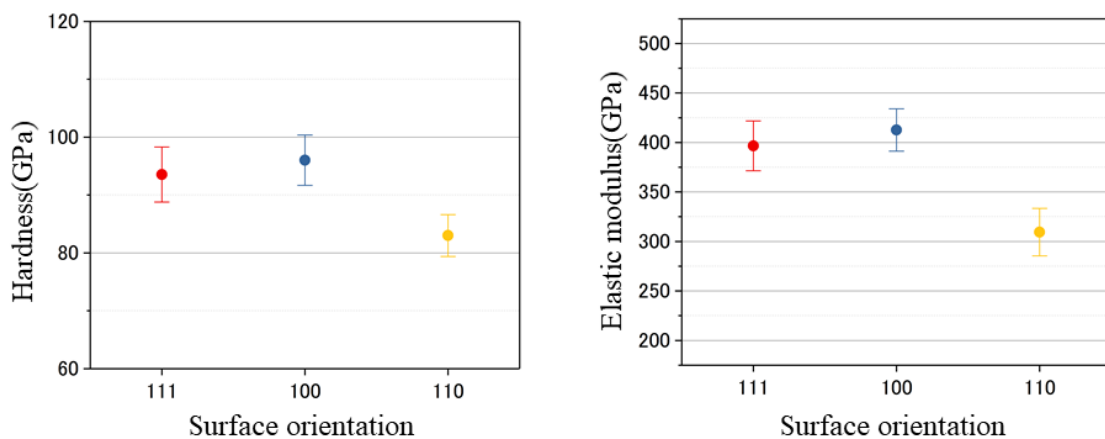


Figure 5-8. Summary of hardness and elastic modulus of 15 specimens. Average angular deviation were  $11.9^\circ$  for (111),  $13.5^\circ$  for (100) and  $14.9^\circ$  for (110).

### 5.3.4 Mechanical Properties Near Grain Boundary

The results of the mapping measurement of hardness and elastic modulus near the grain boundary are shown in Fig. 5-9(b). The mapping was performed by

dividing the  $50 \times 50 \mu\text{m}$  region into  $8 \times 8$  (Fig. 5-9(a)), and hence the spatial resolution is about  $7 \mu\text{m}$ .

At some point in the vicinity of the grain boundary, the hardness and elastic modulus decreased extremely. The hardness at this point was 23.14 GPa and the elastic modulus was 184.6 GPa.

Moreover, from the load displacement curve of the point where this phenomenon occurred, no pop-in phenomenon was seen from this place (Fig. 5-10). It means that the change to the plastic deformation behavior is occurring soon after loading starts.

From these results, it is considered that slip dislocations that greatly affect the hardness and elastic modulus of the crystal are easily generated in the vicinity of the grain boundary.

In order to examine this in more detail, a 3D model was constructed (Fig. 5-11(b)). From the crystal information obtained from EBSD (Fig. 5-11(a)), it was found that the pair of crystals being bonded has a plane symmetrical in the (111) plane direction. Therefore, this sample is considered to be a twin having a plane symmetrical in the (111) direction. It was also found that the twin plane runs obliquely to the substrate surface. The place where the extreme decrease of hardness and elastic modulus occurred is the place where the twin plane exists below. Therefore, it is thought that dislocation such as (111) slip in the twin plane was likely to occur.

Details of the mechanical properties of twin boundary of cBN have not been reported. This experiment revealed for the first time that twin boundary affect as a

factor to greatly reduce the mechanical properties of crystals.

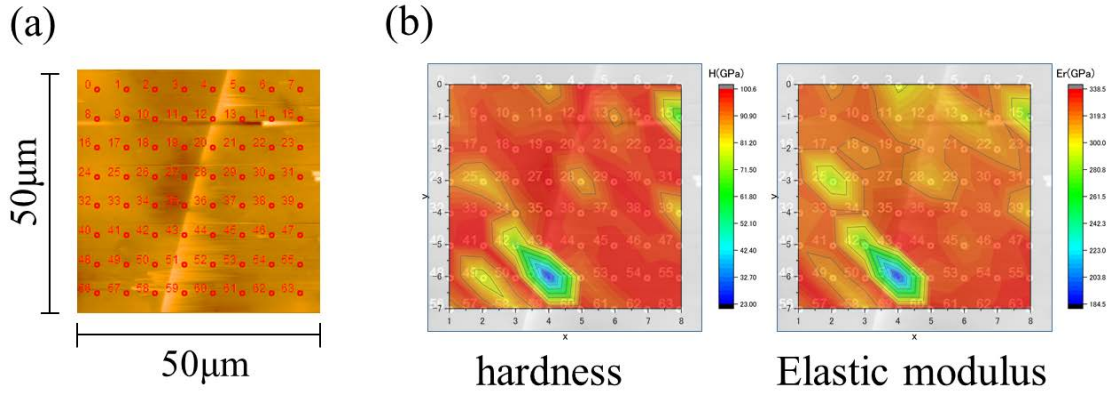


Figure 5-9. (a) Mapping region and measuring point. (b) Mapping data result of hardness and elastic modulus near the grain boundary.

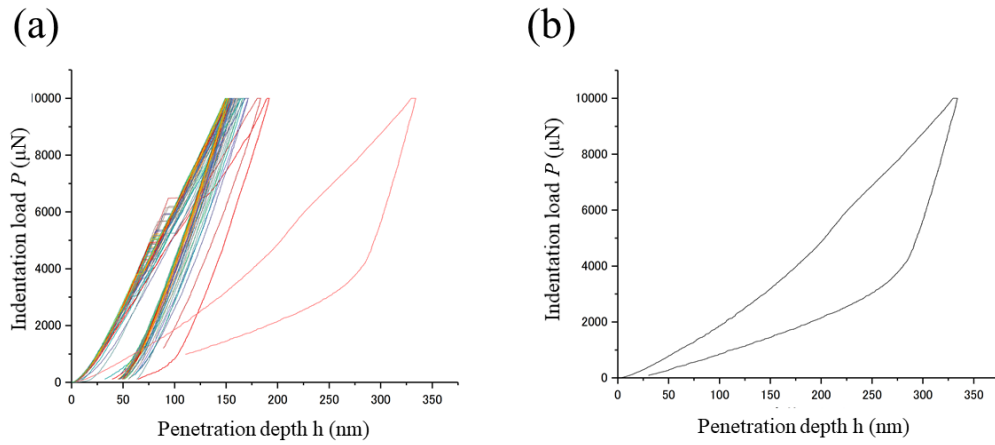


Figure 5-10. (a) Summary of load penetration curves near the grain boundary (64 points). (b) Extract results near the grain boundary.

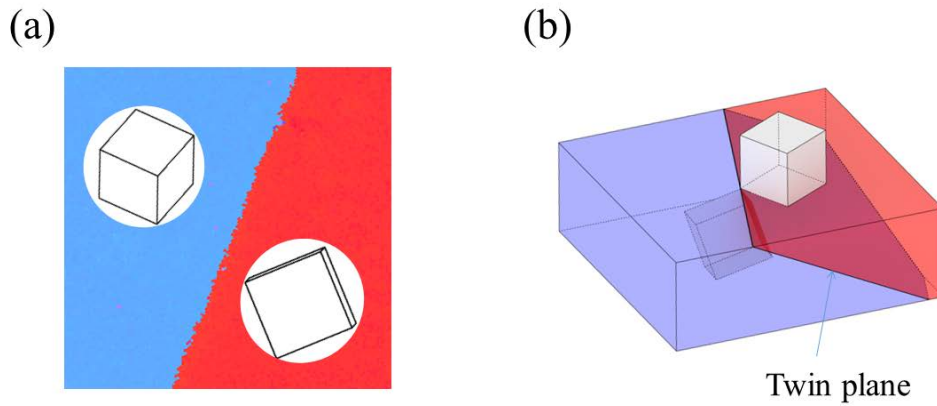


Figure 5-11. (a) EBSD mapping result near grain boundary. (b) 3D model based on EBSD result.

## 5.4 Conclusion

In Chapter 5, a method of nanoindentation was established to investigate the mechanical properties of cBN single crystals. I first experimentally clarified the hardness and elastic modulus on the surface with various index including (111) surface of cBN single crystals. As a result of measuring the samples with 15 random orientations, the hardest face was (100) and it was found that the elastic modulus showed the same tendency. These results confirmed theoretical predictions that (111) dislocation defects are unlikely to occur in the (100) plane.

In addition, the mechanical properties near the twin boundary were clarified for the first time by the mapping measurement. It was found that dislocation generation is easily induced in the vicinity of the twin and thus greatly lowers the mechanical strength. It was found that twins greatly affect the physical properties of the whole crystal.

To summarize, I have measured the precise mechanical parameters of various directions of cBN single crystals. These parameters will be useful for designing the cutting tools in nano-scales and MEMS using piezo electric cBN.

## References

- [1] M. Deura, K. Kutsukake, Y. Ohno, I. Yonenaga, and T. Taniguchi, *Phys. Status Solidi Basic Res.* **1700473**, 1 (2017).
- [2] V.I. Kovtun and V.I. Trefilov, *Sov. Powder Metall. Met. Ceram.* **28**, 903 (1989).
- [3] T. Taniguchi, M. Akaishi, and S. Yamaoka, *J. Am. Ceram. Soc.* **79**, 547 (1996).
- [4] D. M. Teter, *MRS Bull.* **23**, 22 (1998)
- [5] H. Sumiya, Y. Ishida, K. Arimoto, and K. Harano, *Diam. Relat. Mater.* **48**, 47 (2014).
- [6] J.S. Zhang, J.D. Bass, T. Taniguchi, A.F. Goncharov, Y.Y. Chang, and S.D. Jacobsen, *J. Appl. Phys.* **109**, (2011).
- [7] M. P. D. Evelyn, T. Taniguchi, *Diam. Relat. Mater.* **8**, 1522 (1999).
- [8] K. Kim, W.R.L. Lambrecht, and B. Segall, *Phys. Rev. B* **53**, 16310 (1996).
- [9] K. Shimada, T. Sota, and K. Suzuki, *J. Appl. Phys.* **84**, 4951 (1998).
- [10] W. M. Hayers, and D. R. Lide, *CRC Handbook of Chemistry and Physics* (CRC Press, Boca Raton) 91st ed., p. 12-224.
- [11] J. Narayan and A. Bhaumik, *Metall. Mater. Trans. A*, **47**, 1481 (2016).
- [12] C. Huang, X. Peng, T. Fu, Y. Zhao, C. Feng, and Z. Lin, *Appl. Surf. Sci.* **392**, 215 (2017).

## Chapter 6 General Conclusions

In this thesis, I have succeeded in synthesizing a new diamond-related material by developing a new doping method in diamond CVD. I also succeeded in studying detailed properties of the cBN by establishing a new experimental methods for handling sub-mm size single crystal grains.

In chapter 2, I explained the solid immersion doping technique as a new doping method for the diamond. As a result of solid immersion doping of boron, it was found that sufficiently high concentration doping for superconducting transition is possible. As a result, the choice of elements mixed in the diamond has been broadened, opening up the possibility of synthesizing new doped diamond. High concentration or local ( $\delta$ ) doping for the diamond has become possible, which is considered to be effective in making a device with more complicated structural control. In addition, since use of toxic and explosive gas use can be avoided, search for new doped diamonds can be performed more safely.

In Chapter 3, the method developed in Chapter 2 was improved to insert Bi, an element with low melting point. As a result of various analysis, I succeeded in synthesizing substances with a core - shell like structure containing bismuth as nuclei in the diamond film. From this result, I found that the solid immersion doping method is effective as a method to create a substance with a new nano structure.

In Chapter 4, I established a polishing technique to prepare surfaces with arbitrary crystallographic indexes of sub-mm grains. This method was applied to cBN single crystals with widely available sizes. This solved the difficulty in

obtaining a single crystal substrate for experiments. It became possible to conduct detailed surface scientific experiments of single crystals which are unknown in many points. I also investigated the surface reaction of cBN single crystal in plasma and clarified the etching mechanism. As a result of investigating the reactivity of cBN to several gas species, I found a gas species that has an effect of anisotropic etching useful for device application.

In Chapter 5, a detailed study of mechanical properties was carried out for the first time using cBN microcrystals. cBN single crystal plates with various crystallographic orientation were prepared using precision polishing technique. Nanoindentation test was conducted to investigate mechanical properties such as hardness and elastic modulus. A "pop-in" phenomenon in which the indenter tip suddenly subsides was observed for the first time in the cBN. I have elucidated the mechanical properties which have been known only from polycrystalline film, sintered body, theoretical calculation, and established a method to find effective information for improving the performance of MEMS devices and cutting tools made of cBN.

I am closing this thesis by stating future prospects of this research. In Chapters 2 and 3, a new technique to explore the doped diamonds have been established. I hope this technique will be widely used to synthesize new doped diamond with multiple doping including vacancies, which has not been studied well up to now. In Chapters 3 and 4, it has become possible to prepare cBN surfaces with arbitrary crystallographic indexes. With the precise study of plasma-surface interface such has been presented in this thesis, it will become possible to discover a gas phase

synthesis technique for high quality cBN films for device applications. I hope electronic/optical/mechanical circuits will be realized in the future from the combination of these new experimental techniques for the diamond and cBN.

## **Acknowledgements**

I would like to give heartfelt thanks to Prof. T. Shimada who provided research environments, carefully considered feedback and valuable comments to my research. I would also like to thank Prof. A. Wakeshima and Prof. T. Nagahama who gave me invaluable comments and warm encouragements.

I am grateful to Prof. R. Nowak for assistance of research, living and moral support when staying in Finland and Dr. P. Jalkanen for development of the new method of nanoindentation and Dr. M. Trebara for teaching me how to use the indentation equipment.

I would like to thank T. Takami for collaborator in the experiments with high precision techniques for three years.

I gratefully acknowledge the work of past and present members of the laboratory.

I would also like to express my gratitude to my family for their moral support and warm encouragements.